

Assessing urban surface thermal environment and heat health risk in Chinese cities: A twenty-year study



Chunxiao Zhang ^a, Yang Yang ^{a,*}, Le Yu ^{b,c,d,**}

^a School of Information Engineering, China University of Geosciences, Beijing 100083, China

^b Department of Earth System Science, Ministry of Education Key Laboratory for Earth System Modeling, Institute for Global Change Studies, Tsinghua University, Beijing 100084, China

^c Ministry of Education Ecological Field Station for East Asian Migratory Birds, Beijing 100084, China

^d Tsinghua University (Department of Earth System Science)- Xi'an Institute of Surveying and Mapping Joint Research Center for Next-Generation Smart Mapping, Beijing 100084, China

ARTICLE INFO

Keywords:

Heat health risk
Local climate zone (LCZ)
Land surface temperature retrieval
Urban heat island (UHI)
Urban morphology

ABSTRACT

With global warming and rapid urbanization, urban surface temperatures have risen significantly, challenging residents' health and urban sustainability. Prolonged or frequent high temperature exposure can cause various health issues, making the study of heat-related risks crucial. However, data accessibility issues and other factors limit the temporal and spatial scales of studies. This insufficiently considers intra-urban spatial heterogeneity, hindering detailed exploration of urbanization's impacts on heat risk. Therefore, this paper evaluates the surface thermal environment and heat health risks in Chinese urban areas from 2000 to 2020 using the IPCC's "hazard-vulnerability-exposure" framework. It proposes a method to analyze these patterns at a 100-m resolution among different LCZ types. Results show that heat risks have increased over the past 20 years, with higher risks in the northwest, southeast, and central regions. Built-type LCZs, especially those with high building density and height, have significantly higher heat risks than natural-type LCZs. LCZ 8 and LCZ 10 exhibit relatively high heat risk levels, though lower than dense building zones. In contrast, areas with vegetation (LCZ A-D) and water bodies (LCZ G) show significantly lower heat risks compared to other LCZ types. The paper proposes targeted heat adaptation strategies and planning recommendations based on these findings.

1. Introduction

As global climate change and urbanization accelerate, climate issues in urban environments have increasingly drawn widespread attention. Particularly in many large cities, factors such as dense buildings, lack of vegetation cover, and waste heat generated by human activities often lead to the so-called "urban heat island effect," where temperatures within the city are higher than those in surrounding suburban areas. This phenomenon not only affects residents' quality of life but also has negative impacts on public health, energy consumption, and ecosystems. Rapid urbanization and intensive human activities have significantly altered the characteristics of surface materials (Song et al., 2020), for example, increasing the use of concrete and asphalt, which have high heat retention

* Corresponding author at: School of Information Engineering, China University of Geosciences, Beijing 100083, China.

** Corresponding author at: Department of Earth System Science, Ministry of Education Key Laboratory for Earth System Modeling, Institute for Global Change Studies, Tsinghua University, Beijing 100084, China.

E-mail addresses: yangyangdida@163.com (Y. Yang), leyu@tsinghua.edu.cn (L. Yu).

capacities. Natural elements such as vegetation have been replaced by impermeable materials and buildings (Yang and Zhao, 2023), adversely affecting the urban ecological environment, altering the urban thermal regime, and exacerbating the urban heat island (UHI) effect in most cities (Macintyre et al., 2021; Xue et al., 2022; Yuan et al., 2022).

This phenomenon not only affects daily living comfort but can also have negative impacts on health. According to a report by the World Health Organization (WHO), high temperatures are one of the leading environmental factors contributing to non-communicable deaths. At the same time, due to climate change, the number of extreme temperature events, including heatwaves, is increasing annually. Based on current trends, this number is expected to nearly double between 2001 and 2030 (Reduction and f. D. R., 1901). Regardless of absolute temperatures, heatstroke and death can occur outside designated extreme events. Prolonged or frequent exposure to high-temperature environments may induce various health issues, such as cardiovascular diseases, respiratory illnesses, and renal failure (Soneja et al., 2016; Wang et al., 2023). The impact is particularly significant for vulnerable groups like the elderly and children, who are more sensitive to heat (Campbell et al., 2018; Belmin et al., 2007; Kenny et al., 2010).

Heat health risk refers to a type of heat-related health risk, which indicates the spatial proximity between populations and heat hazards (Romero-Lankao et al., 2012). High-temperature health risk assessment is an effective tool for understanding and reducing heat-related morbidity and mortality (Sun et al., 2024). Mapping heat health risks is crucial for preventing and addressing the negative impacts of heat hazards, improving urban environments, and promoting sustainable development. Meanwhile, based on the correlation analysis between Local Climate Zone (LCZ) classification results and heat health risks, a new zoning approach suitable for urban heat health risk management is proposed. This approach addresses some limitations of previous analyses and governance methods that were based on administrative units. Managing health risks associated with the urban heat island effect has also become an important new research direction. Comprehensive risk identification and assessment, along with reasonable risk mitigation strategies, hold significant practical importance for urban management (Nie et al., 2021). Therefore, investigating heat-related health risks is highly necessary. An increasing number of studies are focusing on this area as a means of climate adaptation (Xie et al., 2024; Muccione et al., 2024; Zhu and Yuan, 2023; Xiang et al., 2024a). However, accurately assessing the specific high-temperature risks faced by individuals or groups in practice and providing corresponding protective recommendations requires scientific analysis based on extensive data.

Early research on the impact of high temperatures on human health primarily focused on the pathological studies of health hazards caused by high temperatures. (Åström et al., 2011) With continuous development, heat health risk assessment has now been refined to comprehensively consider factors such as population vulnerability. The Crichton Risk Triangle framework is currently widely used in health risk assessments related to heat. This framework aligns with the disaster risk assessment system proposed in the IPCC Fifth Assessment Report (Field et al., 2014; Crichton, 1999), which is based on ‘hazard exposure—social vulnerability—exposure.’ It re-defines exposure as elements or entities (e.g., people, infrastructure, and assets) that are specifically exposed or at risk, separating exposure from vulnerability. This distinction addresses the inadequacies in early research where exposure was considered a component of vulnerability, leading to insufficient adaptation measures. This framework continues to be employed in the Sixth Assessment Report (Michelozzi and De’Donato, 2021). Recent studies have demonstrated that heat risk assessments based on this framework are scientific and reliable (Estoque et al., 2020; Pramanik et al., 2022), providing guidance for our heat health risk assessments.

Over the past two decades, improvements in data availability, computational processing and storage capabilities, as well as advancements in geospatial analysis technologies, have enabled the potential for spatial assessments (Anselin, 2012). Human susceptibility to high temperatures varies across different spatial scales (Wolf et al., 2015). Given China’s vast territory, significant regional differences and varying economic levels necessitate a multidimensional comprehensive assessment. Mapping heat risk at national, urban, and intra-urban scales is a crucial theme of this study’s heat risk evaluation. Additionally, the difficulty in obtaining long-term data related to heat risk, the complexity of methodologies, and the high demand for interdisciplinary collaboration have resulted in relatively few studies on long-term time series of heat risk (Xu et al., 2024). This research conducts a comprehensive long-term series heat risk assessment for major urban areas across China from 2000 to 2020.

Meanwhile, most previous studies on urban thermal environment assessment have used ‘administrative units’ (such as districts, streets, or communities) as the spatial scale and attempted to discover the thermal environment patterns within each administrative unit in a city (Walton et al., 2016). Although these risk assessments based on administrative units are useful for urban planning and management (Estoque et al., 2020), the actual distribution within these administrative boundaries is often quite uneven (Bao et al., 2015). Urban thermal environment research based on administrative boundaries fails to capture the relationship with the internal structure of the city more precisely, making it difficult to link risks with specific urban planning measures. Fortunately, the LCZ classification scheme proposed by Stewart and Oke has created a bridge that connects urban built environments, urban spatial morphology, and urban climate characteristics research. As LCZ-related research has progressed, many studies have found that the LCZ classification system can serve as a powerful tool for analyzing urban thermal environments, thermal comfort, and heat risk (Johnson and Jozdani, 2019; Verdonck et al., 2018; Lau et al., 2019; Verdonck et al., 2019). In previous long-term heat health risk assessment work, it may have been challenging to conduct large-scale long-term assessments due to the spatial and temporal limitations of LCZ datasets. Fortunately, our previous LCZ mapping project team jointly mapped 100-m resolution LCZ datasets for major urban areas in China from 2000 to 2022. This makes it possible for this paper to explore urban thermal environments and heat health risks over a long time series at the LCZ scale. Additionally, the assessment of heat health risks is conducted with a spatial resolution of 100 m, which enhances the precision of our calculations.

In summary, the accelerated urbanization process and global climate change have introduced complex and variable urban microclimate conditions. Against this backdrop, scientifically understanding and assessing the health risks posed by excessively high or low temperatures to the public in different locations and time periods has become an urgent and deeply explored issue. Therefore, establishing a reasonable and effective system for precise prediction and monitoring across different spatial scales (from macro to micro) and temporal scales is crucial.

This study will conduct long-term observations of urban thermal environments and heat health risks based on issues such as time span, spatial span, and research scale, incorporating multi-source remote sensing data and geospatial big data, utilizing frameworks such as the Crichton risk triangle. It aims to provide a more comprehensive framework by describing indicators within traditional large-scale regional divisions and various urban areas. Using Local Climate Zones to investigate urban heat-related health risks at a fine spatial scale aims to reveal the spatiotemporal distribution and evolution trends of heat risks across different spatial areas, analyze the variations in heat risks among different LCZ types, and explore the feasibility of using LCZs as analytical units for heat-related health risk analysis. This approach helps deepen the understanding of the relationship between LCZs and heat-related health risks. Furthermore, it provides scientific evidence for urban planning and public health decision-making through the formulation of climate adaptation strategies.

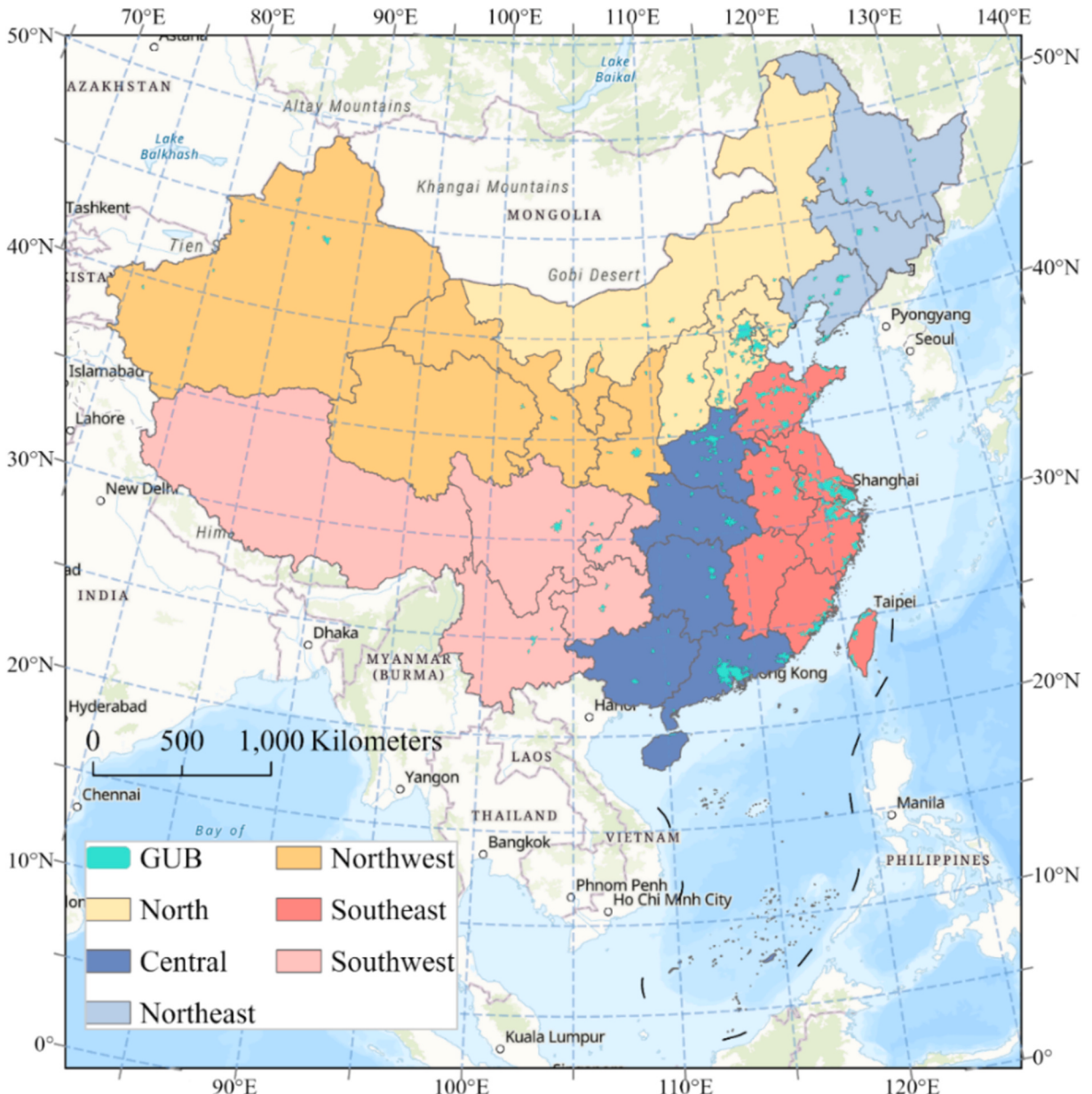


Fig. 1. Spatial Distribution Map of the Study Area.

2. Data and methods

2.1. Study area

Our LCZ map dataset was created using a partitioning approach, dividing China into six regions based on geographical factors: Northeast, North China, East China, Northwest, Southwest, and Central South. Training samples from different regions were used to classify cities within these areas based on the Global Urban Boundaries (GUB) dataset. This study continues this methodology, aiming to conduct thermal environment and heat health risk assessments as well as pattern analyses at both regional and urban scales across the entire country. The division method of the six major regions and the location range of city boundaries are shown in Fig. 1.

2.2. Data collection and preprocessing

All the data used in the experiment are listed in Table 1, which specifies the purpose of each type of data and the specific experimental modules they are involved in.

3. Methods

3.1. Technical route

All the technical routes used in the experiment are shown in Fig. 2, mainly including three aspects.

LCZ Mapping: This task was completed previously with members of our research group. The mapping process involved several steps including LCZ classification, urban change detection, temporal consistency filtering, and result aggregation to obtain the final version of the LCZ map.

LST Inversion: Based on data from Landsat 5 and Landsat 8, this study utilized the PSC algorithm to derive an annual summer average Land Surface Temperature (LST) dataset with a spatial resolution of 100 m for the GUB region over the period from 2000 to 2020.

Heat Health Risk Assessment: Following the hazard-exposure-vulnerability framework proposed by the IPCC, this part of the study evaluates heat health risks. By integrating the results from LCZ mapping, LST inversion, and heat health risk assessment, we aim to analyze and identify the final spatial pattern trends.

3.2. LCZ classification mapping

Most existing LCZ products either map only a single year or separately map multiple years. Due to the challenges of mapping urban morphology, such as the large workload of collecting multi-year samples, lack of high-resolution images, and achieving temporal consistency in LCZ time series, creating long-term sequences of urban morphology remains an area that needs further exploration. This paper adopts an improved LCZ classification system (Zhao et al., 2023), which includes four main steps for obtaining annual LCZ datasets:

LCZ Classification: Based on Sentinel and Landsat remote sensing imagery, preprocessing steps such as cloud removal synthesis, PCA, normalization, etc., are conducted. Two texture features (sum average and difference) of the gray-level co-occurrence matrix (GLCM) are extracted. Within the Global Urban Boundaries (GUB) dataset range, Random Forest classification and validation are performed based on features like NDVI, MNDWI, texture, nighttime lights, DEM, etc.

Rule-based Filtering: An empirical rule is established to restrict changes in urban morphology within possible ranges. This step eliminates classification errors and ensures temporal consistency.

Table 1
Data Sources.

Data Name	Source
Landsat-5/8	LANDSAT/LC08/C02/T1_L2 LANDSAT/LT05/C02/T1_L2
MODIS LST	MODIS/061/MOD11A1
Relative Humidity	https://www.geodata.cn/main/
Wind Speed	https://www.geodata.cn/main/
Total Population Density	WorldPop/GP/100 m/pop
Nighttime Lights Data	https://dataverse.harvard.edu/dataset.xhtml?persistentId=doi:https://doi.org/10.7910/DVN/GIYGJU https://hub.worldpop.org/geodata/listing?id=30
Elderly and Child Population Density	(>80 years & <4 years)
NDVI	MODIS/061/MOD13Q1
MNDWI	LANDSAT/LC08/C02/T1_L2 LANDSAT/LT05/C02/T1_L2
Annual PM 2.5/10	https://data.tpdc.ac.cn/home
LCZ	https://zenodo.org/records/10444179

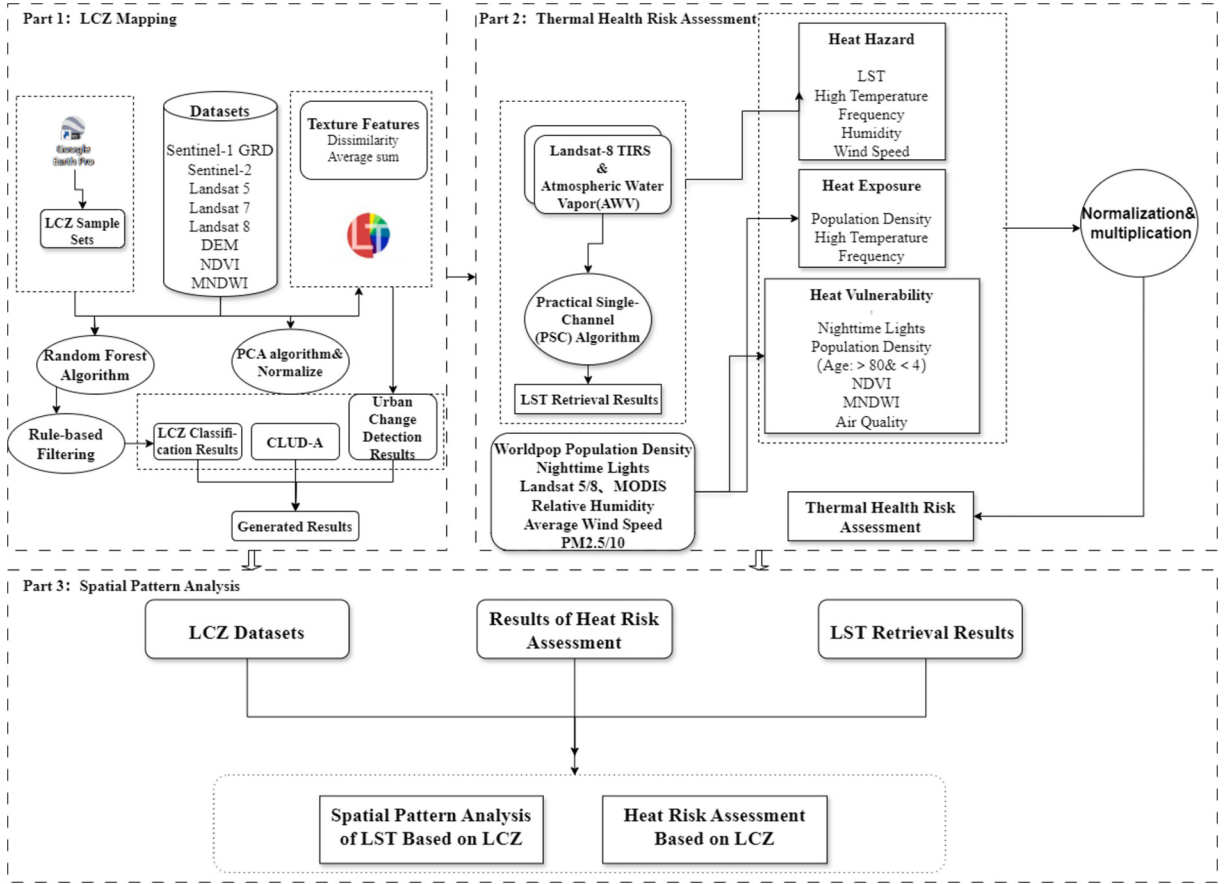


Fig. 2. Technical Route Diagram.

Urban Change Detection: To mitigate error accumulation effects, a method combining texture features and the Landtrendr algorithm (based on Landsat's disturbance and recovery trend detection) is used for detecting urban change areas, thereby limiting changes in urban morphology regions.

Result Aggregation: Finally, the filtered LCZ maps, urban change detection results, and existing land cover maps (CLUD) are aggregated to derive the final urban morphology time series.

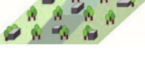
The specific meanings of all LCZ types mentioned in this study are shown in Table 2.

3.3. LST retrieval

Currently, most researchers opt to use LST obtained from satellites or temperatures acquired from ground stations to describe heat hazard indices. Although the air temperature measurements retrieved from meteorological stations reflect the actual temperatures perceived by people, the limited number of monitoring stations results in insufficient spatial resolution of the obtained LST data (Chen et al., 2022), making it challenging to conduct high-precision experiments. In contrast, LST data acquired through remote sensing satellites typically have higher spatial resolution, overcoming these limitations (Peng et al., 2018). Since existing research has already demonstrated a very good correlation between LST and air temperature (T2m) (Cheval et al., 2022; Cheval et al., 2023), and since the urban microclimate represented by LST better reflects relative mortality risk compared to air temperature (Avashia et al., 2021), we have chosen to use LST as the temperature indicator in our study. The Moderate Resolution Imaging Spectroradiometer (MODIS) LST products offer a relatively balanced temporal and spatial resolution and are widely used for health risk assessments related to heat (Cao et al., 2019). However, this study aims to analyze the spatial and temporal patterns of the thermal environment and heat health risks from an LCZ perspective. Therefore, the LST dataset requires high spatial resolution. Additionally, the quality of remote sensing images is often affected by clouds, haze, and other weather conditions, leading to image gaps.

To address this, we will retrieve summer LST annually from 2000 to 2020 based on Landsat remote sensing imagery and calculate the average results. Wang et al. have experimentally demonstrated that their proposed single-channel framework based on atmospheric water vapor (AWV)-dependent PSC algorithm can retrieve high-precision Landsat LST datasets in a simple and stable manner (Wang et al., 2020; Wang et al., 2019). Hence, this paper adopts the PSC method using Landsat-5 TM band 6 and Landsat-8 TIRS band 10 along with atmospheric water vapor content data to compute the annual summer LST averages from 2000 to 2020. The formulas

Table 2
LCZ classification system in our study (adapted from (Stewart and Oke, 2012)).

LCZ 1	LCZ 6	LCZ A	LCZ F
Compact high-rise	Open low-rise	Dense trees	Bare soil or sand
			
LCZ 2	LCZ 7	LCZ B	LCZ G
Compact mid-rise	Lightweight low-rise	Scattered trees	Water
			
LCZ 3	LCZ 8	LCZ C	LCZ H
Compact low-rise	Large low-rise	Bush , scrub	wetland
			
LCZ 4	LCZ 9	LCZ D	
Open high-rise	Sparingly built	Low plants	
			
LCZ 5	LCZ 10	LCZ E	
Open mid-rise	Heavy industry	Bare rock or paved	
			

used for the calculations are [Formula 1](#) and [Formula 2](#).

$$LST = c_2 / \lambda \ln(c_1 / \lambda^5 B(T_s) + 1) \quad (1)$$

$$B(T_s) = a_0 + a_1 \omega + (a_2 + a_3 \omega + a_4 \omega^2) \frac{1}{\epsilon} + (a_5 + a_6 \omega + a_7 \omega^2) (L_{sen} / \epsilon) \quad (2)$$

Among them, LST represents the land surface temperature that needs to be retrieved. λ represents the effective wavelength. $B(T_s)$ represents the Planck radiation at temperature. a_k ($k = 1, 2, 3, \dots$) represents the correlation coefficients of the Landsat dataset. L_{sen} represents the sensor radiance. ω represents the atmospheric water vapor content (AWV). ϵ represents the land surface emissivity.

3.4. Heat health risk assessment

According to the previous review of the heat health risk assessment framework, this paper uses the Crichton risk triangle concept framework promoted by the IPCC to quantify and estimate the impact of heat-related health risks. It mainly includes three parts: heat hazard, heat exposure, and heat vulnerability. After reviewing the literature and considering data availability, this paper decides to select the following indicators to describe the components of the three risk elements.

$$V' = 0.1 + (0.9 - 0.1) \times (V - Min) / (Max - Min) \quad (3)$$

$$V' = 0.1 + (0.9 - 0.1) \times (Max - V) / (Max - Min) \quad (4)$$

To ensure comparability between indicators and to be able to aggregate at the indicator and framework levels, this paper standardizes all indicators. Considering that different indicators have varying directions of influence on heat hazard, heat exposure, and heat vulnerability, [formula 3](#) is used for the standardization of positive indicators, where higher values indicate higher heat risk. [Formula 4](#) is used for the standardization of negative indicators, where lower values indicate higher risk. The above standardization formulas not only consider the direction of the indicator's impact on heat risk but also avoid zero and negative values (Dong et al., 2020; Xiao et al., 2023), controlling the standardized results within the range of 0.1–0.9 to facilitate the subsequent aggregation of various indicators in calculating heat health risk.

$$HRI = hazard \times exposure \times vulnerability \times 1000 \quad (5)$$

The final Heat Risk Index (HRI) is calculated by multiplying the three normalized components (heat hazard, heat exposure, and heat vulnerability) with equal weights. This is because the methods section of the paper assigns equal importance to each component's influence on the heat risk index (Paranunzio et al., 2021), resulting in all factors being given equal weights. Additionally, several previous studies have employed the product of equally weighted three indicators within the risk triangle framework to assess heat risk, demonstrating the validity of this approach (Wu et al., 2024). Previous scholars have also suggested that the multiplicative principle better reflects the complex relationships between indicators compared to the additive principle (Estoque et al., 2020; Hu et al., 2019). To make the final HRI index calculation results more intuitive, the product result is multiplied by 1000 to obtain the final HRI index. The calculation formula is Formula 5.

3.4.1. Heat Hazard

A hazard is defined as a “potential occurrence of a natural or human-induced physical event, trend, or impact that may lead to loss of life, injury, or other health impacts, as well as damage and losses to property, infrastructure, livelihoods, service provision, ecosystems, and environmental resources” (Michelozzi and De' Donato, 2021).^[22] Surface temperature directly affects the thermal load on the environment. High surface temperatures can cause air temperatures to rise, thereby increasing the risk of human exposure to high-temperature environments, so surface temperature is used to represent air temperature (Amani-Beni et al., 2022).

High-temperature frequency refers to the number of days with high temperatures occurring each summer. Frequent high-temperature events increase the probability of heat-related illnesses and deaths, while also putting stress on infrastructure and ecosystems. Since evaporation of sweat is a basic function for lowering body temperature (Sherwood and Huber, 2010), relying solely on temperature data might not fully represent the perceived heat discomfort in assessing heat hazards in different regions (Im et al., 2019), especially in hot and humid areas. Relative humidity indicates the percentage of water vapor content in the air. It, together with air temperature, determines the apparent temperature, i.e., the actual temperature felt by humans. Lower relative humidity increases evaporation and transpiration, leading to potential human water resource shortages (Denson et al., 2021). In high-humidity environments, the efficiency of body cooling through sweating decreases, making it easier to suffer from heatstroke and other heat-related health issues, thus increasing the degree of heat hazard.

Wind speed influences air movement, thereby affecting heat transfer and evaporative cooling processes. Higher wind speeds help dissipate heat by promoting sweat evaporation, reducing the degree of heat hazard. Previous studies have shown that temperature, humidity, and wind speed all affect human comfort levels. Heat comfort conditions depend not only on temperature changes but also on humidity and wind speed trends (Ginzburg et al., 2024; Solaimani et al., 2024). Therefore, LST, high-temperature frequency, relative humidity, and average wind speed are identified as descriptive indicators of heat hazard.

For the calculation of the LST indicator, the summer average LST from 2000 to 2020 is calculated from Landsat images to represent the LST indicator. For the calculation of high-temperature frequency, we will use the definition of hot weather provided by the National Meteorological Administration and utilize MOD11A1 Terra Land Surface Temperature data to count the number of days each summer with temperatures exceeding 35 °C (Ma et al., 2023). The MOD11A1 data provides daily daytime LST data at a resolution of 1000 m. Using daily data allows for more accurate statistics on the occurrence of high-temperature weather. After completing the calculations, the four heat hazard indicators need to be resampled to 100 m to ensure spatial resolution compatibility with other data. The final calculation formula for the heat hazard indicator is Formula 6.

$$\text{heatHazard} = (T + F + H + W)/4 \quad (6)$$

T stands for surface temperature, F stands for high-temperature frequency, H stands for relative humidity, W stands for average wind speed.

An unweighted quantitative aggregation (addition) and normalization of indicators to a 0–1 range is a common method (Hossain, 2001). This approach has been widely adopted in indicator construction because it helps to avoid additional subjectivity. Furthermore, several studies on heat health risk assessment have employed equal weighting for averaging when refining triangular framework indicators (Xie et al., 2024; Cheval et al., 2023; Dong et al., 2020). In our research, we aim to consider as many descriptive indicators as possible that might affect the heat risk index without engaging in complex physical mechanism calculations. Therefore, the unweighted quantitative aggregation method is more suitable for the analysis in this paper.

3.4.2. Heat exposure

Heat exposure is composed of population density and high-temperature frequency. The IPCC (Intergovernmental Panel on Climate Change) defines “exposure” as the situation where people, properties, systems, or other elements are in areas that could be affected by hazards. High temperatures and heatwaves in areas with higher population densities can lead to higher heat-related mortality rates (Medina-Ramon and Schwartz, 2007). Therefore, population density (the larger the number of people, the greater the likelihood of being exposed to high temperatures) and high-temperature frequency (the more frequent the occurrence of high-temperature weather, the greater the risk of heat health issues) are identified as indicators describing heat exposure.

In selecting population density data, WorldPop gridded population density data provides annual population distribution information at a spatial resolution of 100 m. Compared to other population statistics based on administrative divisions, WorldPop gridded population density data offers higher-resolution population distribution information (Elizabeth Loughnan et al., 2014). Hence, total grid population density is used as one of the exposure indicators. Some studies have demonstrated that high-temperature frequency poses certain risks to population exposure. Although it has already been used to describe the heat hazard index, the possibility of overestimating the risk due to repeated use of the indicator is low (Ma et al., 2023). Thus, high-temperature frequency is also selected

as one of the descriptive indicators for heat exposure.

WorldPop gridded population density data includes total population density information from 2000 to 2020 at a 100-m resolution. High-temperature frequency is calculated using data sources with a 1000-m resolution. To match the spatial resolution of other data, it needs to be resampled to 100 m. The final calculation formula for the heat exposure indicator is [Formula 7](#).

$$\text{heatExposure} = (H + F)/2 \quad (7)$$

H represents the annual total population density and F represents the high-temperature frequency.

3.4.3. Heat vulnerability

Unlike traditional visible light remote sensing, nighttime light remote sensing can capture night-time illumination. The resulting radiance values represent light brightness, which directly reflects the intensity of human activities and sensitively indicates economic vitality and urban development ([Hu et al., 2024](#); [Doll et al., 2006](#)). A region's ability to respond to disasters largely depends on its economic status. Compared to economically disadvantaged areas, residents in wealthier regions have access to better housing conditions, medical resources, public infrastructure, social support, and work environments, making them less vulnerable to heat events. Therefore, this study selects nighttime light data as an indirect representation of socioeconomic variables.

However, the data years for the two major sources of nighttime light data differ: NPP/VIIRS nighttime lights cover 2012–2023, while DMSP/OLS nighttime lights span 1992–2013. Due to differences in spectral resolution, spatial resolution, radiometric resolution, and product update cycles, DMSP-OLS and SNPP-VIIRS data are incompatible, preventing long-term time series analysis from 2000 to 2020 required for this study. Fortunately, researchers have developed algorithms to unify these two types of nighttime light data, demonstrating that the improved DMSP-OLS-like data has great potential for effectively assessing socioeconomic development and human activities ([Wu et al., 2021](#)). This study will use this unified dataset product as the source of nighttime light data.

Meanwhile, elderly individuals and children are more vulnerable to high temperatures ([Yang et al., 2021](#)). On one hand, as people age, their physiological characteristics become increasingly fragile. Elderly individuals' bodies react more slowly to temperature changes, and their sweat gland function may decline, making it harder for them to cool down through sweating. Many elderly people suffer from chronic diseases such as cardiovascular disease and diabetes, which make them more sensitive to high temperatures and increase the risk of heatstroke and other heat-related illnesses. On the other hand, children's thermoregulatory systems, especially those of infants and toddlers, are not fully developed. They have lower heat tolerance and relatively higher metabolic rates, generating more heat but with less efficient cooling compared to adults. Studies indicate that the heat-related mortality risk for individuals over 75 is twice that of younger people ([Cao et al., 2023](#)), and among deaths of people aged 65 and above during specific periods, 61 % were from those aged 80 and above ([Lloyd et al., 2024](#)).

Therefore, population densities of the elderly (over 80 years old) and children (under 4 years old) are selected as indicators of heat vulnerability. The greater the number of such populations in a region, the higher its heat vulnerability. WorldPop provides annual population density datasets for each age group from 2000 to 2020 at a resolution of 100 m, enabling consideration of human physiological vulnerability. Given that elderly people and young children are more sensitive to heat-related health risks due to their more fragile physiological characteristics and lower heat tolerance, the population density of those over 80 and under 4 years old is also chosen as a vulnerability indicator.

In addition, biophysical factors may also contribute to human heat vulnerability. Vegetation reduces surface temperatures through transpiration and shading effects, thereby mitigating the urban heat island effect and reducing heat vulnerability. Water bodies have a high specific heat capacity, which can regulate the surrounding environment's temperature through evaporative cooling; at the same time, water bodies can increase air humidity, helping alleviate the adverse impacts of hot and dry weather on humans. The primary pollutants that most significantly affect human health are PM10 and PM2.5 ([Zhang and Wu, 2017](#)). Compared to other pollutants, the impact of PM2.5 and PM10 pollution is more significant ([Wei et al., 2000](#)).

For example, high vegetation and water coverage rates are generally associated with reduced heat-related mortality because they can absorb heat and thus mitigate high temperatures ([Bowler et al., 2010](#)). Previous studies analyzing the correlation between remote sensing indices and LST have demonstrated that MNDWI (Modified Normalized Difference Water Index) and NDVI (Normalized Difference Vegetation Index) are significantly negatively correlated with LST ([Ma and Peng, 2022](#)). Therefore, MNDWI and NDVI can also serve as indicators for describing heat vulnerability.

In summary, nighttime light data, population density of elderly (>80 years old) and children (<4 years old), NDVI, MNDWI, and the concentrations of PM10 and PM2.5 will be used as indicators of vulnerability. These indicators will first undergo resampling and standardization before calculating the vulnerability index. The final calculation formula for the heat vulnerability indicator is [Formula 8](#).

$$\text{heatVulnerability} = (H + L + N + M + P + Q)/6 \quad (8)$$

where H represents the population density (for those >80 years old & <4 years old), L represents nighttime light intensity, N represents NDVI, M represents MNDWI, P represents the concentration of PM2.5 in the air, and Q represents the concentration of PM10 in the air.

4. Results and analysis

4.1. Spatiotemporal pattern analysis of LST based on LCZ

In the spatiotemporal pattern analysis of LST based on LCZ, this paper takes LCZ as a starting point to examine the temporal patterns of LST in major urban areas across the country from 2000 to 2020, as well as the variations in LST among different LCZ types. To visually demonstrate the spatial distribution of LST in urban areas, and considering the availability of original remote sensing data as well as the typicality of high temperatures in cities, Fig. 3 depict the spatial distribution maps of surface temperature for representative cities from six regions across the country for the years 2000, 2010, and 2020. Due to potential issues with the quality of data sources used for LST retrieval, there may be some missing data for certain years. In such cases, data from years close to the three target years will be used for mapping purposes.

From the images, it can be observed that from 2000 to 2010 and then to 2020, there is an overall upward trend in surface temperature across various cities. The extent of high-temperature areas has continuously expanded, with many regions that were originally cooler turning into high-temperature zones, and low-temperature areas decreasing, especially near city centers. This phenomenon partially reflects the reduction in vegetation and the intensification of the urban heat island effect due to urbanization processes.

However, some regions do not exhibit a consistent increase every year; for instance, the surface temperature in 2010 might be the highest among the three years in certain cities, such as Nanjing. Shenyang, located in the northeastern region, had the lowest surface temperature among all representative cities in 2000. Wuhan, situated in the central region, showed the most significant increase in surface temperature over the 20-year period, having the highest surface temperature among all representative cities in 2020. Among all the representative cities, Wuhan, Chongqing, Nanjing, and Urumqi generally exhibited relatively higher surface temperatures.

Analyzing the spatial distribution patterns of surface temperature within each city, high-temperature areas are typically concentrated in densely built-up zones with frequent human activities, such as city centers, residential areas, commercial districts, industrial zones, and major transportation routes. These areas tend to have higher surface temperatures due to dense construction, paved roads, and intense human activity. Conversely, low-temperature areas are associated with natural environments like green spaces and water bodies, predominantly found in parks, green belts, rivers, lakes, and other water bodies, as well as the outskirts of cities. These regions, covered by abundant vegetation and water bodies, can significantly lower surface temperatures, thereby creating relatively cool “cold islands” within urban settings.

4.1.1. Average summer LST variation patterns by building type

Due to the higher likelihood of elevated LST in urban areas characterized by certain LCZ, Fig. 4 aims to maintain clarity by illustrating the variations in LST differences within built-up LCZ regions from 2001 to 2020, relative to the year 2000. Each colored point represents a specific LCZ type.

Overall, the LSTs for various LCZs have shown a generally increasing trend with fluctuations over the past two decades. Notably,

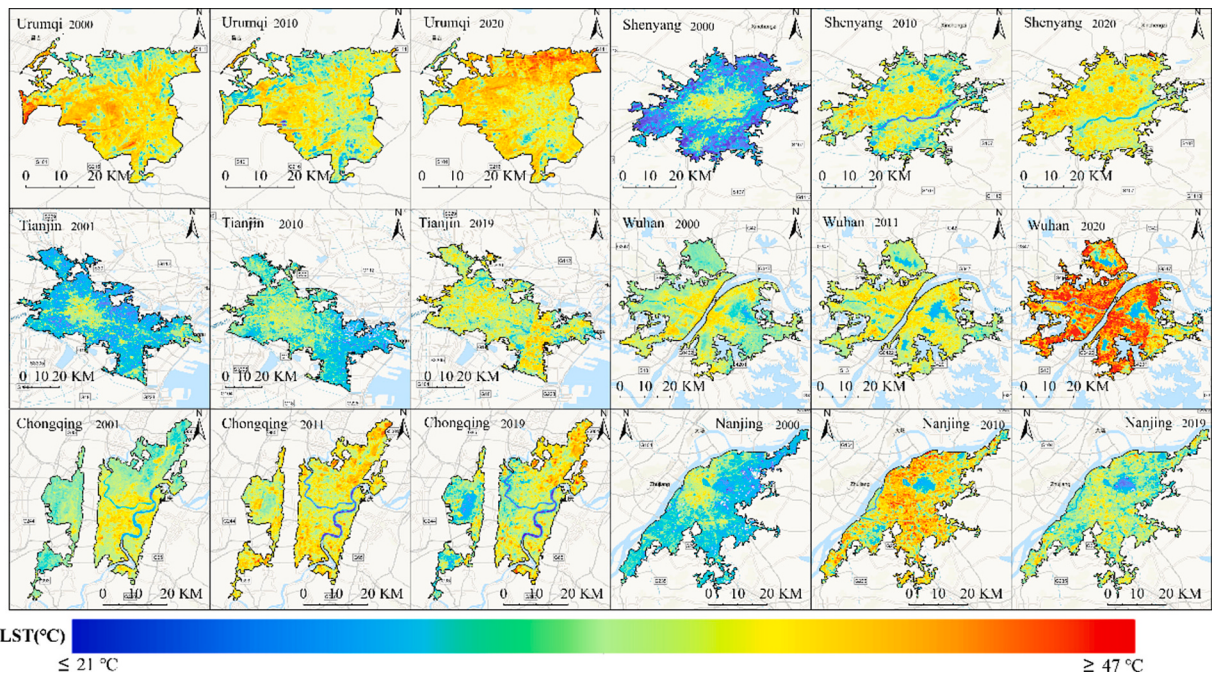


Fig. 3. Spatial Distribution Maps of Surface Temperature in Representative Cities from Different Regions for the Years 2000, 2010, and 2020.

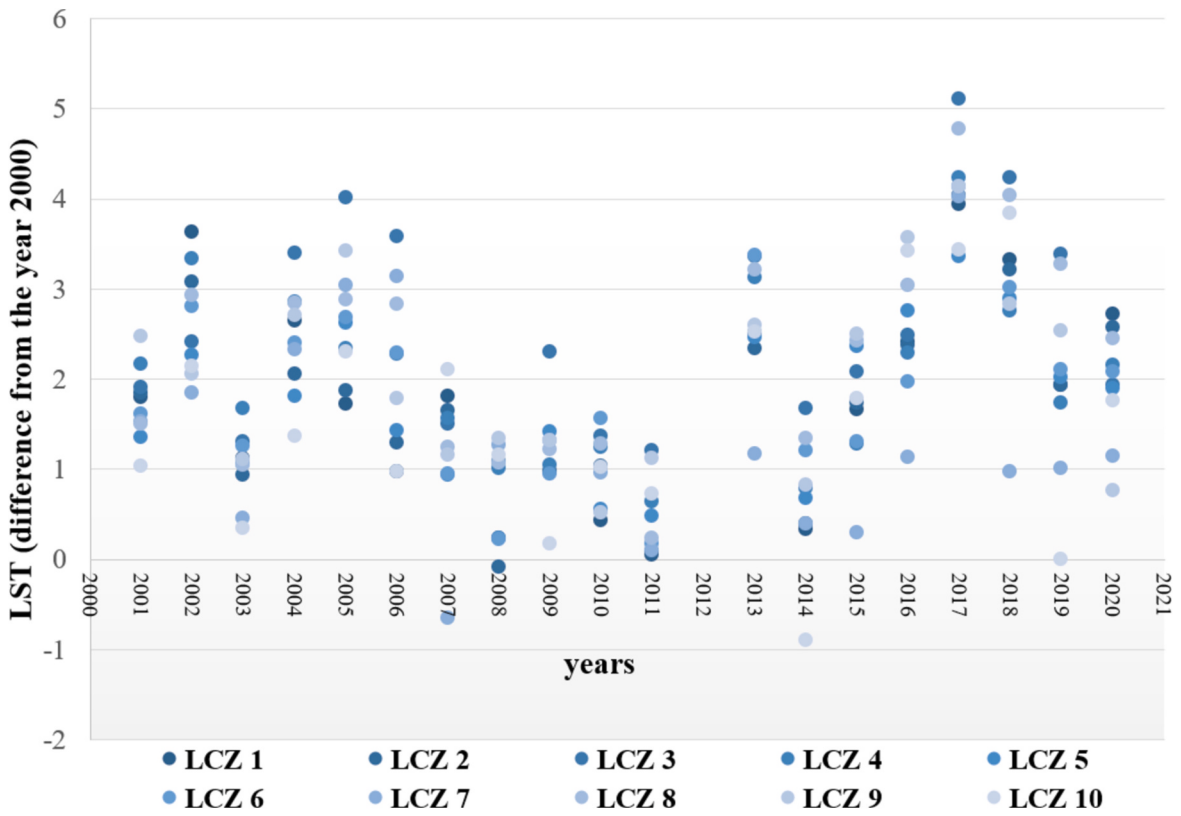


Fig. 4. Variation in the Difference of Average LST between Different LCZ Types from 2001 to 2020 Compared to Data from 2000.

there were significant increases in LST around the years 2005 and 2017 compared to adjacent years. The temperature changes across most LCZ types appear to be synchronous, potentially influenced by global climate events or extreme weather conditions. While each LCZ type exhibits its unique pattern of temperature variation, all demonstrate some degree of annual fluctuation.

Despite fluctuations, the long-term trend, particularly after 2015, indicates a significant increase in LST relative to the year 2000 for most LCZ types. This aligns with the broader context of global warming. In 2016 and 2017, most LCZ types exhibited high positive differences, indicating that the LSTs in these years were relatively higher compared to other years since 2000. This may be attributed to global climate change or localized climatic conditions. Conversely, some LCZ types displayed negative differences in 2014 and 2015, meaning that the LSTs during these years were lower than those in 2000. These trough periods could reflect specific meteorological events or temporary cooling phenomena.

LCZ 1, 2, and 3 represent highly dense urban areas. The graph shows that these zones generally have positive deviations in most years, suggesting more pronounced urban heat island effects and faster changes in surface temperature. In contrast, open-type buildings like LCZ 6 and industrial areas (LCZ 10) exhibit smaller variations in LST, often fluctuating around zero. Additionally, the similar trends in temperature changes across most LCZ types, indicated by the gradient from darker to lighter colors on the scatter plot, further validate the appropriateness of analyzing urban thermal environment spatial patterns at the LCZ level.

4.1.2. Spatial pattern analysis of surface temperature in 2020 and its growth over the past 20 years

To clearly illustrate the spatial distribution patterns of surface temperature for the most recent year and its changes over the past 20 years, we conducted a quantitative bivariate mapping using two cartographic variables: the LST of representative cities in various geographic regions for the year 2020 (or nearby years), and the difference between these values and the corresponding LSTs from the year 2000.

From the Fig. 5, it can be observed that most areas in Tianjin exhibit a relatively high annual increase in surface temperature, with the overall level of surface temperature being moderate among all cities. Urumqi shows relatively low interannual variation in surface temperature, but its overall surface temperature level is comparatively high. Additionally, Urumqi presents a spatial characteristic where peripheral regions have higher absolute values of surface temperature in 2020 and greater growth rates. Shenyang has higher absolute values of surface temperature but lower interannual variation, with these characteristics primarily distributed in the city center. Wuhan and Chongqing have higher absolute levels of surface temperature compared to other cities. Notably, Wuhan features large areas with high temperatures and moderate annual increases as well as areas with high temperatures but lower annual increases, which may reflect varying development efficiencies within different parts of the city. Nanjing also has a relatively high overall surface temperature but exhibits a lower overall growth rate.

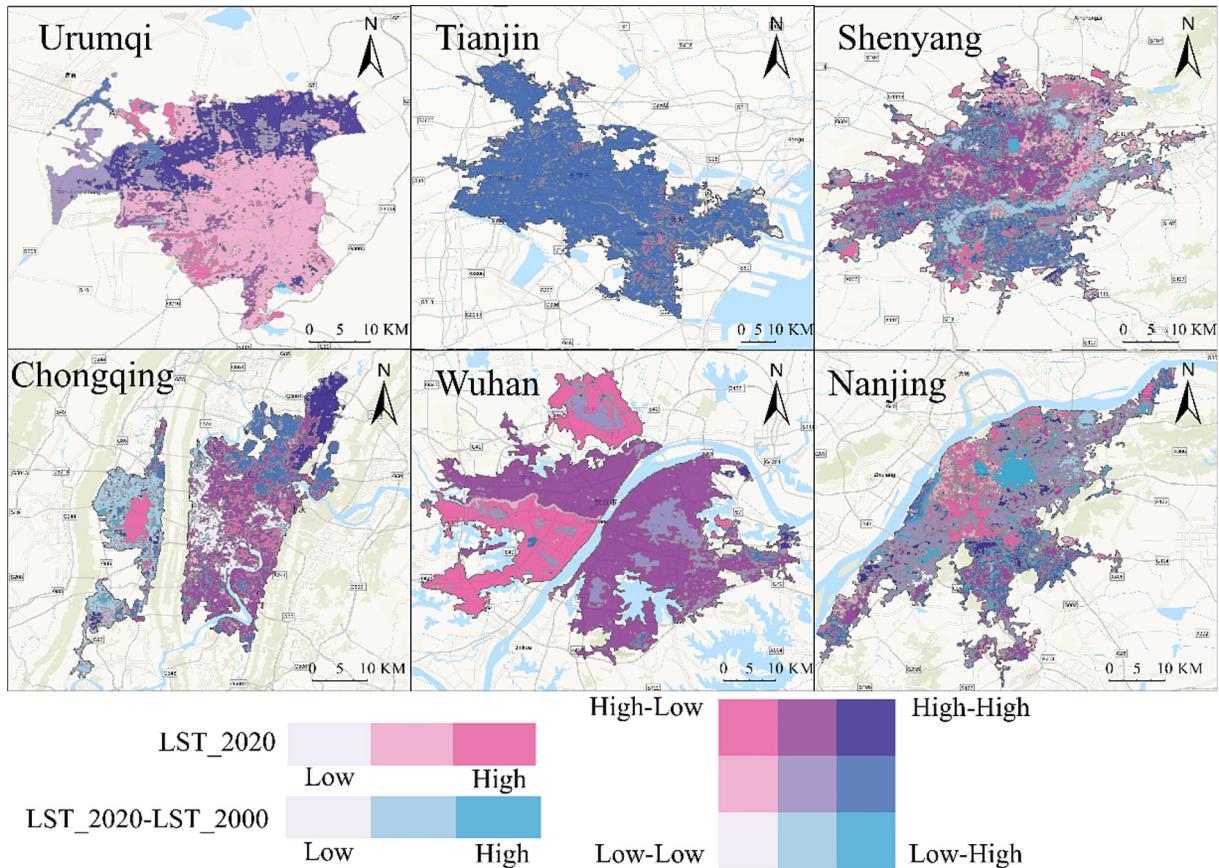


Fig. 5. Bivariate Quantitative Analysis of LST for Representative Cities in 2020 and the Difference with Corresponding Regional LSTs in 2000.

4.1.3. Analysis of LST patterns based on LCZ mapping units

In previous work involving long-term series datasets of LCZ mapping, our research team found that dividing China's urban areas into six major regions (Northwest, North, Northeast, Southwest, Central, Southeast) and using these regions as training units for machine learning algorithms yielded optimal results. Therefore, this paper also considers analyzing the statistical patterns of summer average surface temperatures across these six regions and among different LCZ types, taking 2020 as an example. Fig. 6 shows the mapping results.

Using 35 °C as a reference standard, it can be observed that the surface temperatures in multiple LCZ types exceed 35 °C in the Southeast, Central, and Northwest regions. In contrast, the North and Northeast regions have surface temperatures distributed around the 35 °C reference line, while all LCZ types in the Southwest region are significantly below this reference line. This indicates that urban areas in the Southwest have notably lower surface temperatures compared to other regions nationwide.

Additionally, the statistical results for the Northwest region are somewhat unique. Although most LCZ types fluctuate around the reference line, LCZ 5 and LCZ 7 exhibit relatively higher surface temperatures than other building types. This could be due to intense sunlight exposure in the Northwest, leading to large exposed areas with limited greenery, high proportions of hard surfaces like roads, concentrated human activities, frequent vehicle traffic, and increased heat emissions, further elevating surface temperatures. Moreover, natural types such as LCZ C, LCZ E, and LCZ F also show significantly higher surface temperatures in the Northwest. This may be because these areas lack sufficient vegetation cover under conditions of long summer daylight hours and strong solar radiation, resulting in shrubs, bare soil or sand, and exposed rocks or roads having high thermal capacity and conductivity. They absorb heat quickly during the day and release it slowly at night, causing large diurnal temperature variations and persistently high surface temperatures. Road materials like asphalt and concrete also possess high thermal capacity and conductivity, creating a significant heat island effect.

Overall, densely built-up areas (such as LCZ 1, 2, 3) consistently show higher surface temperatures across all regions, reflecting the presence of the urban heat island effect. Green spaces and water bodies (such as LCZ A, B, G), regardless of the region, typically have lower surface temperatures. These green and water-covered areas help reduce temperatures and mitigate the urban heat island effect.

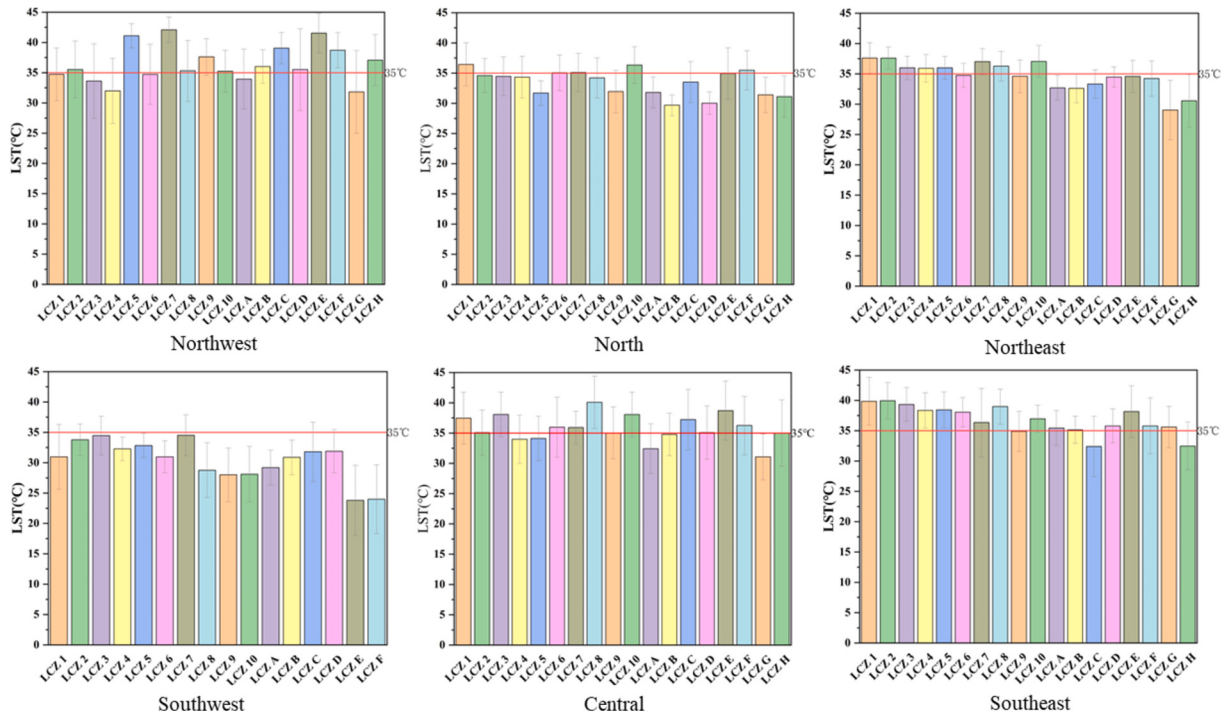


Fig. 6. Analysis of LST Patterns Based on LCZ Mapping Units.

4.2. Heat health risk analysis based on LCZ

In the analysis of spatiotemporal patterns of heat health risk based on LCZ, this study continues to use LCZ as the entry point. It maps the heat health risk index for major urban areas across the country from 2000 to 2020 and conducts statistical analysis of heat health risks from different dimensions. Fig. 7, using representative cities from six regions as examples, visually display the spatial

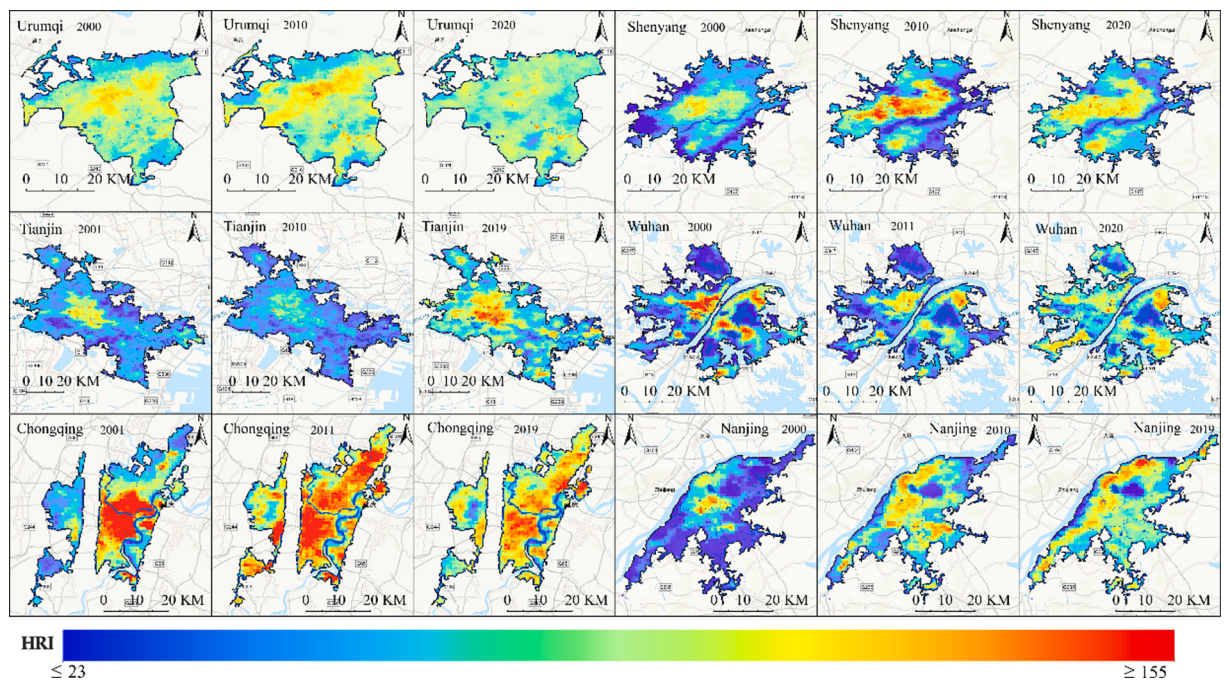


Fig. 7. Spatial Distribution Maps of HRI in Representative Cities from Different Regions for the Years 2000, 2010, and 2020.

distribution patterns and temporal changes of the heat health risk index for the years 2000, 2010, and 2020. To further illustrate the spatial patterns of the three indicators—heat hazard, heat exposure, and heat vulnerability—we have mapped the spatial distribution patterns of these indicators for cities in 2020 as an example (See the Appendix for details).

From the images, it can be seen that Urumqi has a relatively high overall heat risk, but the areas with deep red (indicating highest risk) are few and far between. The distribution of risk levels is fairly uniform without any significantly concentrated high-risk zones. Shenyang exhibits moderate heat risk overall, with higher risks in the central urban area gradually extending outward. In Tianjin, the central urban area also shows higher heat risk which has noticeably intensified over time. In Wuhan, the central urban areas along the Yangtze River exhibit very high heat risk, and the extent of these high-risk areas has significantly expanded from 2000 to 2020. Chongqing stands out among all cities for having the most pronounced heat risk, with large red areas indicating extremely high heat risk across most regions, showing a trend of further expansion. Nanjing's map predominantly features yellow and orange colors, indicating moderately high heat risk, especially in the city center. Over time, the same locations have shown an increasing trend in heat risk levels, with high-risk areas expanding.

Overall, among the six cities, except for Urumqi, the other five cities have experienced an increase in the urban heat island effect, particularly noticeable in Wuhan and Chongqing, reflecting the impact of accelerated urbanization. Additionally, high heat risk areas within each city are primarily concentrated in the city centers and surrounding regions, while the outer areas tend to have relatively lower risk.

4.2.1. Analysis of heat risk level composition based on LCZ

To further analyze the differences in heat risk levels among different LCZ types, this paper classifies heat risk levels into five categories: extremely high, high, moderate, low, and extremely low using the natural breaks method. It also calculates the area composition of different LCZ types' heat risk levels for effective urban areas nationwide in the years 2000, 2010, and 2020. To avoid unfairness caused by directly using area metrics, their percentage compositions were calculated for mapping purposes. Fig. 8 shows the mapping results of percentage composition. Additionally, to provide a more detailed explanation of the contribution levels of the three indicators—heat hazard, heat exposure, and heat vulnerability—to heat risk, we have illustrated the composition of these indicators across different LCZ types for the year 2020(See the Appendix for details).

Overall, the proportion of high and very high heat health risks is significantly higher in building-type LCZs compared to natural-type LCZs. Conversely, the proportion of low and very low heat health risks is much greater in natural-type LCZs than in building-type LCZs. Among building types, the percentage of very high risk is higher in dense buildings (LCZ 1, LCZ 2, LCZ 3) compared to open buildings (LCZ 4, LCZ 5, LCZ 6). Additionally, when the building density is similar, the proportion of very high risk decreases sequentially from high-rise buildings (LCZ 1, LCZ 4), to mid-rise buildings (LCZ 2, LCZ 5), to low-rise buildings (LCZ 3, LCZ 6). The proportion of very high heat risk components in LCZ 8 and LCZ 10 is relatively higher compared to LCZ types such as LCZ 6, LCZ 7, and LCZ 9 within the building type LCZ categories. However, it remains lower than that of dense building types, and the proportion of very high-risk components in LCZ 8 is slightly higher than in LCZ 10.

In natural-type LCZs, areas with lush vegetation (LCZ A, LCZ B, LCZ C, LCZ D) and water bodies (LCZ G) have a significantly higher proportion of very low heat health risk levels. In contrast, bare ground areas (LCZ E, LCZ F) generally exhibit higher heat risk levels, which can even match the proportions of very high and high heat risks found in relatively lower-risk building types. Among the various types of lush vegetation, the denser, taller, and more abundant the trees are, the greater the proportion of very low heat health risk. Meanwhile, the proportion of low-risk areas is overall similar among sparse trees, shrubs, and low-lying vegetation.

In 2000, the proportion of extremely high heat risk and high heat risk levels in all components mostly ranged between 10 %–50 %, with LCZ 1 and LCZ F having a high-risk proportion close to 60 %. By 2010, the proportion of high-risk levels had decreased in many categories, generally ranging from 10 %–40 %. The highest proportions of high-risk components were found in LCZ 10, LCZ 1, and LCZ 2. By 2020, these proportions increased again, particularly evident in LCZ 1, LCZ 2, and LCZ 8 types.

4.2.2. Differences in heat risk across different geographical zones

Fig. 9 summarizes the average Heat Risk Index (HRI) for each natural region from 2000 to 2020. Overall, the trend lines indicate that although the growth rates of HRI values differ across regions, most regions exhibit an upward trend in HRI values between 2000 and 2020. This increase is particularly notable in the Northwest and Southeast regions. In specific years such as 2009, 2012, and 2018,

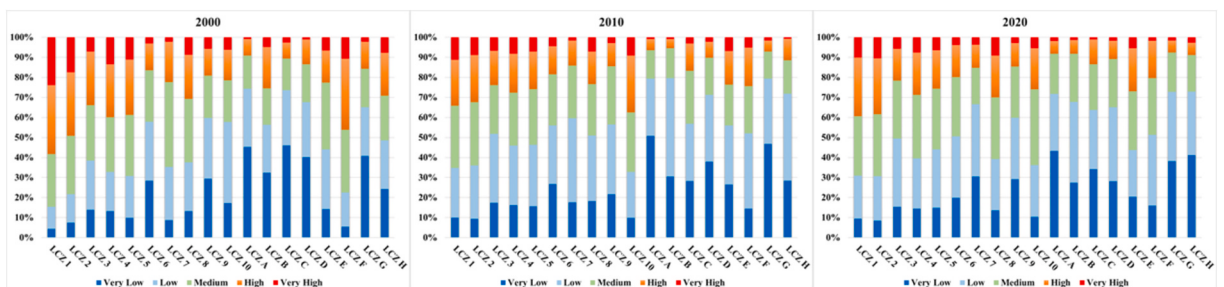


Fig. 8. Component Analysis of Heat Risk Levels for Different LCZ Types.

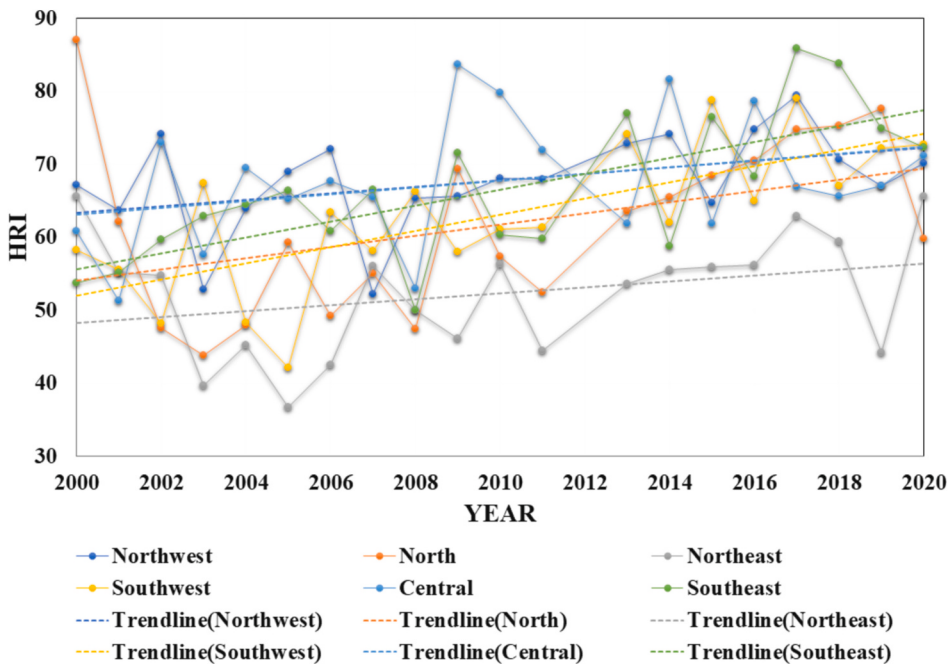


Fig. 9. Statistical Diagram of the Average Heat Risk Index for Six Natural Geographic Regions from 2000 to 2020.

there are noticeable peaks in HRI values across all regions, which may correspond to certain extreme weather events or unique environmental conditions. Regarding growth rates, the Southwest and Southeast regions have experienced the fastest increases in summer average heat risk indices over the past 20 years.

In terms of regional differences in heat risk indices, the Northwest, Southeast, and Central regions generally show higher HRI values, often exceeding 70, indicating a higher heat risk in these areas. There are distinct differences in HRI values among regions: before 2012, the Central and Northwestern regions had higher heat risks; from 2013 to 2016, the Southwestern and Southeastern regions exhibited relatively higher heat risks. From 2017 to 2020, the heat risk in the Southeastern and Northern regions began to rise significantly, surpassing other regions. Meanwhile, the Northeastern region has consistently shown lower HRI values over the past 20 years, remaining below the average level, though it has seen some recovery after 2010.

4.2.3. Differences in heat risk across different geographical zones

Moran's I index is the most commonly used metric to quantify spatial autocorrelation and helps characterize the spatial aggregation of geographic features (Lam et al., 2018). In this study, both global and local Moran's I indices were employed to represent the spatial autocorrelation of Heat Risk Index (HRI), aiming to identify the spatial clustering phenomena of heat health risks within various urban areas. The results of the global spatial autocorrelation analysis for the 2020 HRI in each city indicate significant positive spatial autocorrelation across all cities, with clustering patterns showing that high-risk areas influence their surrounding regions. The calculated results presented in Table 3 demonstrate a notable spatial clustering in the HRI, exhibiting high levels of statistical significance ($p < 0.001$).

To conduct a more detailed analysis of local spatial aggregation patterns, a local Moran's I analysis was further employed. The k-nearest neighbors (KNN) algorithm was used to define spatial weights (with $k = 8$), ensuring the same number of neighboring areas were considered in all calculations, regardless of the size and number of neighbors (Ho et al., 2018).

The calculation results shown in Fig. 10 further confirm the significant spatial clustering of HRI, with high-high clusters being predominant. Overall, in the six cities analyzed, the “high-high” cluster types of Local Moran's I are primarily distributed in central urban areas, while the “low-low” cluster types are mainly located around the periphery of the cities and near natural land cover types

Table 3
Global Moran's I Calculation Results for Representative Cities in Different Geographic Divisions.

City	Global Moran's I	Z-score	P value
Urumqi	0.935393	498.510557	<0.001
Shenyang	0.971925	578.882015	<0.001
Tianjin	0.967586	818.402850	<0.001
Wuhan	0.951443	619.782269	<0.001
Chongqing	0.957919	509.135584	<0.001
Nanjing	0.958270	538.090907	<0.001

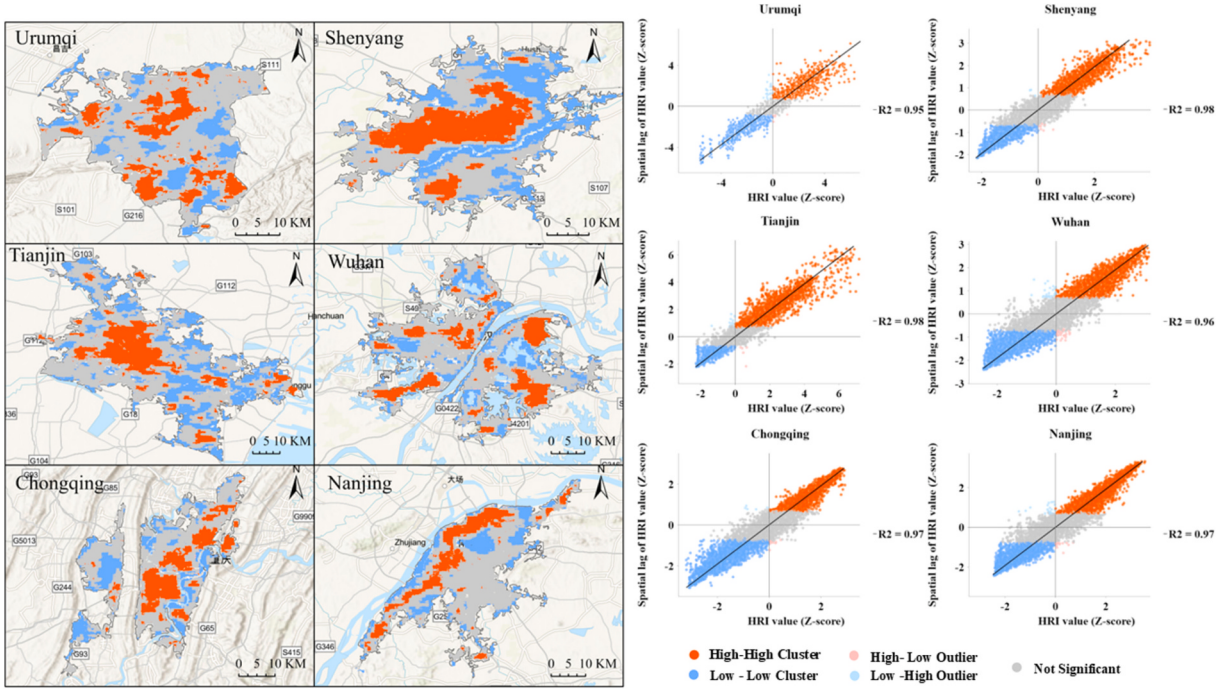


Fig. 10. Local Moran's I Calculation Results for Representative Cities in Different Geographic Divisions in 2020.

such as water bodies.

In Urumqi, the “high-high” clusters are concentrated in developed central urban areas like the High-tech Zone, Tianshan District, and Shayibake District, whereas the “low-low” clusters are predominantly found in regions such as reservoirs (e.g., Salt Lake, Hongyan Reservoir), botanical gardens, or parks (e.g., Junfa Hongguangshan Botanical Garden, Shuimogou Park). In Shenyang, the clustering effect is more pronounced, with two large “high-high” clustering areas. The “low-low” clusters exhibit a distribution pattern along the Hun River that traverses the city. Tianjin also shows clear clustering patterns, with “high-high” clusters mainly located in the Heping and Nankai districts, and “low-low” clusters situated on the city’s outskirts. In Wuhan, the “high-high” clusters are primarily found in central urban areas such as Hanyang, Jianghan, Wuchang, Qingshan, and Hongshan, while “low-low” clusters are mainly along the Yangtze River and around East Lake and Tangxun Lake. In Chongqing, the “high-high” clusters are concentrated in Yubei District, Jiangbei District, Shapingba District, and Jiulongpo District. There is a notable trend of “low-low” clustering in Banan District in the western part of Chongqing and along the Yangtze River. In Nanjing, the “high-high” clusters are primarily located in Jiangning District and Jianye District, following a similar trajectory to the Yangtze River. The “low-low” clusters continue to be aligned along the riverbanks, with a significant “low-low” clustering effect observed in the Purple Mountain area.

5. Discussion

This study uses LCZ as an entry point and analyzes the spatial and temporal patterns of urban heat environments and heat health risks in major cities of China from 2000 to 2020 based on the heat hazard-heat exposure-heat vulnerability risk assessment framework. Furthermore, it verifies that the LCZ classification system can indeed serve as an analytical unit for heat-related health risks. This helps deepen the understanding of the relationship between LCZs and heat-related health risks and provides information for urban planning through the formulation of climate adaptation strategies.

5.1. Contribution of LCZ to heat risk

In previous studies on heat risk at the administrative unit scale, it was not possible to capture the relationship with the internal structure of cities in finer detail. The spatial resolution provided by the LCZ classification system offers urban planners and policy-makers a more comprehensive information base regarding heat risks. According to the experimental results in this study, building-type LCZs exhibit significantly higher heat risk characteristics compared to natural-type LCZs across the country. Dense buildings and high-rise structures have higher heat risks, consistent with previous research findings.

LCZ types such as LCZ 1, LCZ 2, LCZ 4, LCZ 5, LCZ 8, and LCZ 10 show markedly more areas with very high and high heat risk levels, with LCZ 1 and LCZ 2 being particularly prominent (Xiang et al., 2024b). This is consistent with earlier experiments. The overall heat risk for LCZ 3 is higher than that for LCZ 1 and LCZ 2, indicating that building height has a positive effect on heat risk. This may be because high-rise buildings are more likely to absorb and store solar radiation and, due to their height, obstruct wind flow, making it

difficult for heat to dissipate. Meanwhile, LCZ 3 might have more greenery and open spaces compared to LCZ 1 and LCZ 2; these plants help cool through transpiration and provide shade, thereby reducing overall temperatures.

Additionally, LCZ 8 and LCZ 10 also display relatively high heat risks, which deviates from some experimental results suggesting lower heat health risks due to lower population density and human activity (Xiang et al., 2022). However, this study considers multiple factors in addition to LST and population density, including humidity, wind speed, economic level, concentrations of air pollutants, as well as the presence of water bodies and vegetation. In such areas, relatively high heat risks are attributed to the combined effects of higher heat hazards and heat vulnerability.

Among natural-type LCZs, LCZ A, LCZ B, LCZ C, LCZ D, and LCZ G show significantly more areas with very low and low risk levels. This could be because these zones have a relatively high proportion of low SUHI (Surface Urban Heat Island) effects. Green spaces and water bodies within these LCZs effectively mitigate SUHI through shading, transpiration, and greater specific heat capacity (Xiang et al., 2021). Among them, LCZ A and LCZ G have the lowest heat risks, indicating that denser vegetation distribution and larger water body areas correlate with lower heat risk levels. On the other hand, LCZ E and LCZ F show significantly higher heat risks than other natural types, possibly due to bare soil or sand and exposed rocks or roads lacking sufficient vegetation cover. These surfaces have high heat capacity and thermal conductivity, absorbing heat quickly during the day and releasing it slowly at night, resulting in large diurnal temperature variations and persistently high surface temperatures.

5.2. Future urban planning design recommendations

This study further demonstrates the rationality and necessity of formulating high-temperature mitigation strategies from the perspective of LCZ for urban planning and design. Against the backdrop of escalating high-temperature risks, there is an urgent need for targeted urban planning and environmental strategies to alleviate these risks. In the LCZ heat risk analysis concerning natural types, it is evident that areas with high vegetation and water coverage have significantly lower heat risks. Therefore, increasing greenery levels and water body coverage should be considered when formulating strategies.

Dense building zones (LCZ 1, LCZ 2, and LCZ 3) exhibit significantly higher heat risks compared to open building zones. This is primarily due to high building density, poor ventilation, and lack of sufficient greenery in these areas. For dense buildings, greening the rooftops or implementing vertical greenery can be considered (Sharma et al., 2018; Fu et al., 2022). For example, planting lawns or setting up gardens on building tops not only beautifies the environment but also effectively reduces solar radiation absorption. Additionally, utilizing building exterior walls for vertical greening, such as climbing plants or green wall systems, can effectively improve air quality and reduce the urban heat island effect (Wang et al., 2022). Furthermore, using reflective materials like light-colored, high-reflectivity paints or materials to cover roofs and external walls can significantly reduce heat absorption. In new rounds of planning and construction, natural ventilation through open structures and window layouts that allow free airflow should be given more consideration. Additionally, large low-rise buildings (LCZ 8) and heavy industrial areas (LCZ 10) exhibit relatively high heat risk within the LCZ types of building types, though lower than that of dense built-up areas. These areas could benefit from increased factory area greening, such as planting trees and lawns around factories and warehouses to reduce industrial heat release. Establishing green barriers between industrial and residential areas can help mitigate heat diffusion. Enhancing exhaust and waste heat treatment to reduce industrial thermal loads on the environment is also necessary, for instance, promoting energy-efficient equipment and processes to lower energy consumption.

Additionally, among natural LCZs, bare rock and roads (LCZ E) and bare soil and sand (LCZ F) also present high heat risks. Thus, addressing these areas during urban construction is crucial by focusing on vegetation coverage and moisture management. Planting drought-resistant plants in suitable regions can reduce surface temperatures, while artificial irrigation or other methods to increase surface humidity can lower temperatures. Where feasible, enhancing connectivity between green plants (LCZ A, LCZ B, LCZ C, LCZ D) and water bodies can further mitigate the urban heat island effect and reduce heat risks (Peng et al., 2022).

On a national scale, the Northwest and Southeast regions exhibit the highest heat risk. The heat risks in these two areas stem from different climatic characteristics: one is characterized by dry heat, while the other experiences humid heat. Both conditions pose significant threats to human health. People living or working in these regions need to take special precautions against heat stress, such as staying hydrated, avoiding prolonged outdoor activities, and using air conditioning or other cooling devices.

5.3. Limitations of the study

This study primarily has three key limitations:

Firstly, the high-resolution LST data used in this paper is derived from original Landsat imagery. Due to clouds, weather conditions, and the sensors themselves, some areas within the GUB region lack available effective imagery. This results in missing data for LST and subsequently the final HRI index dataset in a few regions. Future research could consider using alternative data sources or employing machine learning algorithms to fill in these gaps.

Secondly, there is currently no unified and universally accepted method for calculating various risk indicators. In our study, we adopted a simple averaging approach to calculate each indicator, assigning equal importance and weight to these factors. While this may not always fully align with specific situations, it serves as a good compromise to address the lack of localized studies and to obtain meaningful generalizations at the national level. Future research needs to establish a more scientific and rational system for selecting indicators and normalization methods. This should consider the physical mechanisms between different indicators as much as possible, aiming to better describe the health threats posed by high temperatures through various indicators.

Finally, the experimental time frame of this study spans from 2000 to 2020, representing a long-term series. Only average summer

LST was used as an indicator due to the revisit cycle of Landsat imagery. As a result, it was not possible to account for variations in heat risk between different months of summer, between day and night, and at various times of the day. Considering more detailed temporal differences would provide better insights into daily heat risk variations, helping people make informed decisions about their travel plans.

6. Conclusion

From the perspective of various natural geographical regions in our country, the northwest and southeast regions as well as the central region have a higher heat risk. These areas generally have higher levels of urbanization and stronger ultraviolet radiation. The northern and southwestern regions have moderate heat risk, while the northeastern region has lower heat risk. This could be due to its high latitude position, which results in relatively less solar radiation, lower air humidity, and larger diurnal temperature variations, making extreme high temperatures less likely to occur in summer; thus, the heat risk is lower.

Additionally, experiments have shown that from 2000 to 2020, as China's urbanization process accelerated, the level of urbanization in various regions nationwide increased. Consequently, the urban heat island effect has also intensified, leading to an overall upward trend in heat health risks. Each type of LCZ exhibits stable patterns and regularities. Overall, the heat risk for built-up LCZ types is significantly higher than that for natural LCZ types.

Specifically, within the built-up types, dense building types (LCZ 1, LCZ 2, LCZ 3) usually exhibit higher heat risks, while open building types (LCZ 4, LCZ 5, LCZ 6) tend to have relatively lower temperature ranges. High-rise buildings (such as LCZ 1) show higher heat risks compared to low-rise buildings (such as LCZ 3). Additionally, large low-rise buildings (LCZ 8) and heavy industrial zones (LCZ 10) exhibit relatively high heat risk levels, though lower than dense building zones. In contrast, within natural LCZ types, areas with vegetation cover (LCZ A-D) and water bodies (LCZ G) have significantly lower heat risks than areas without vegetation and water cover, such as bare rock and paved surfaces (LCZ E) and bare soil or sand (LCZ F).

CRediT authorship contribution statement

Chunxiao Zhang: Writing – review & editing, Supervision, Methodology, Conceptualization. **Yang Yang:** Writing – original draft, Visualization, Investigation, Data curation. **Le Yu:** Writing – review & editing, Supervision, Methodology, Conceptualization.

Declaration of competing interest

The authors declare that they have no conflict of interest.

Acknowledgment

This work was supported by the National Natural Science Foundation of China (grant number 42371425).

Appendix A

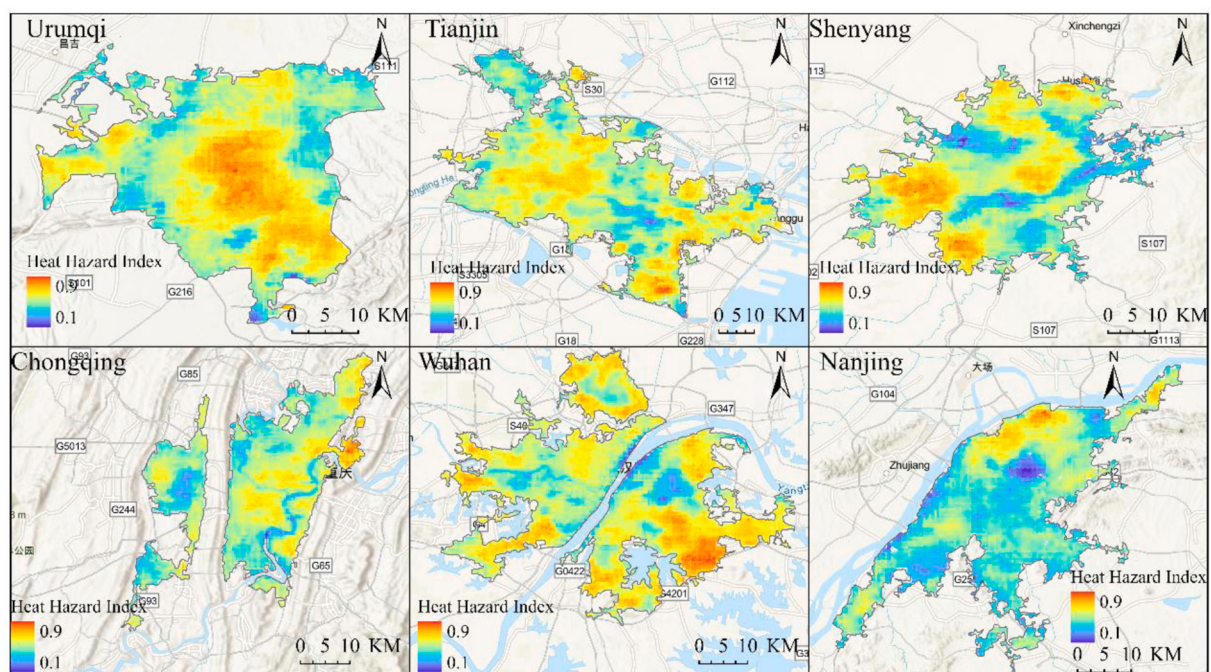


Fig. A. Heat Hazard Index Calculation Results for Representative Cities in Different Geographic Divisions in 2020.

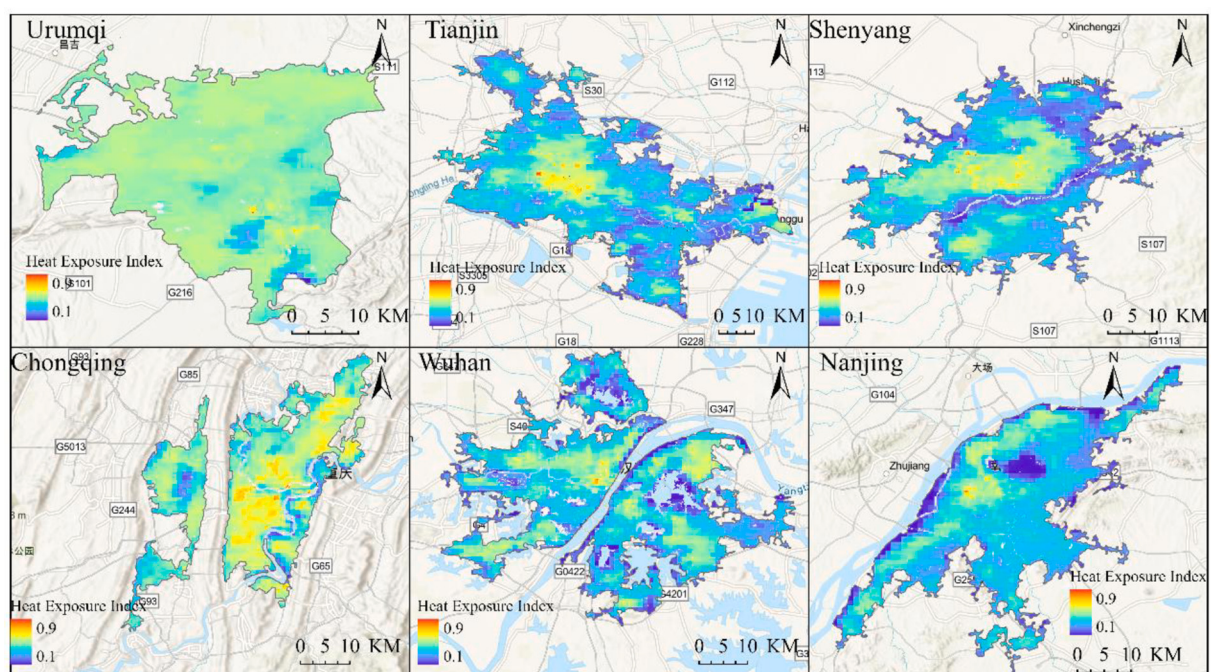


Fig. B. Heat Exposure Index Calculation Results for Representative Cities in Different Geographic Divisions in 2020.

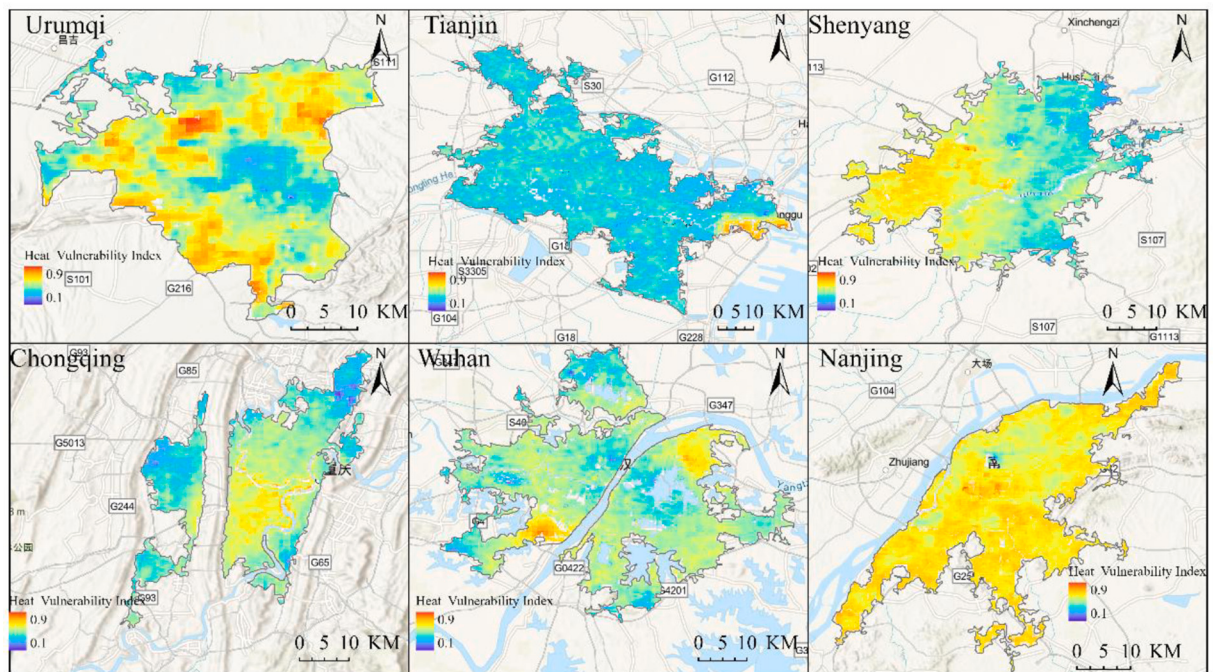


Fig. C. Heat Vulnerability Index Calculation Results for Representative Cities in Different Geographic Divisions in 2020.

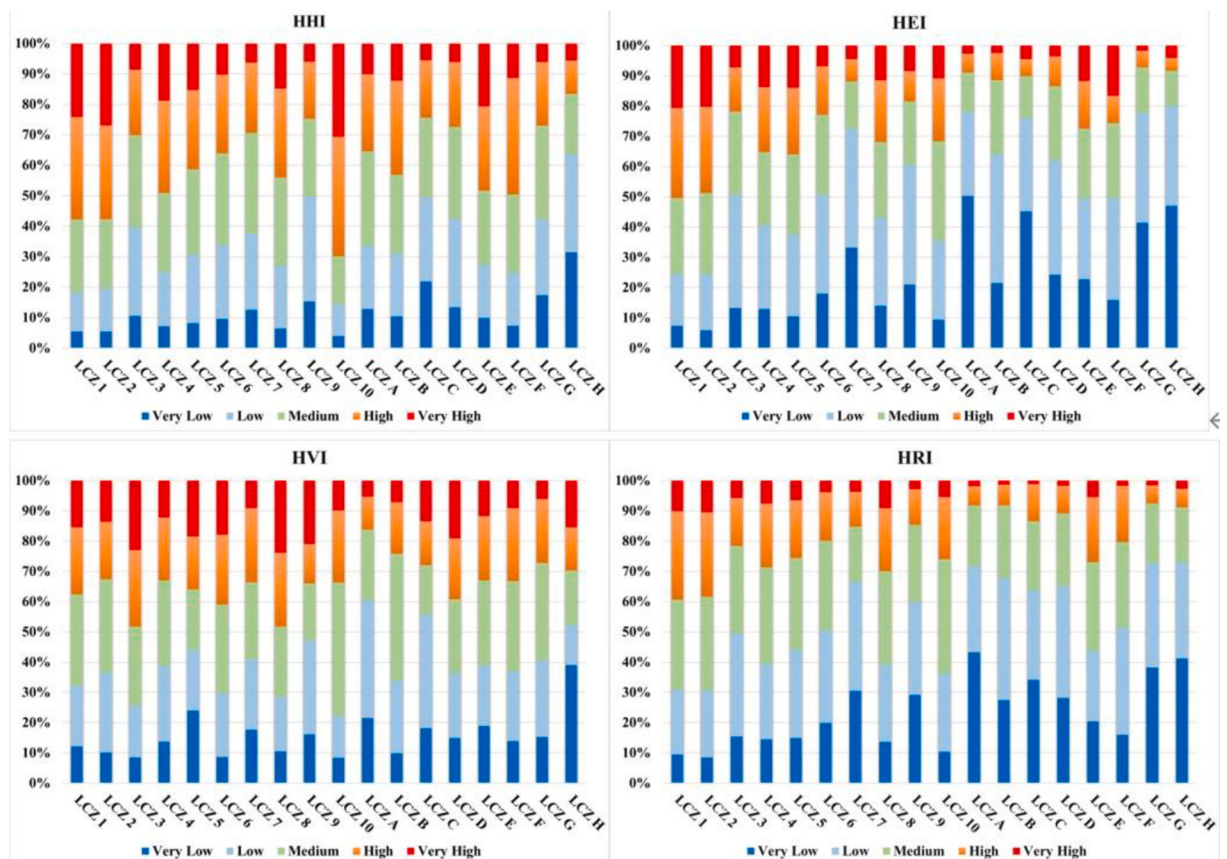


Fig. D. Proportion of Different Levels of Heat Hazard Index (HHI), Heat Exposure Index (HEI), Heat Vulnerability Index (HVI), and Final Heat Risk Index (HRI) in Different LCZ Types in 2020.

Data availability

Data will be made available on request.

References

- Amani-Beni, M., Chen, Y., Vasileva, M., Zhang, B., 2022. Quantitative-spatial relationships between air and surface temperature, a proxy for microclimate studies in fine-scale intra-urban areas? *Sustain. Cities Soc.* 77, 103584.
- Anselin, L., 2012. From SpaceStat to CyberGIS: twenty years of spatial data analysis software. *Int. Reg. Sci. Rev.* 35 (2), 131–157.
- Åström, D.O., Bertil, F., Joacim, R., 2011. Heat wave impact on morbidity and mortality in the elderly population: a review of recent studies. *Maturitas* 69 (2), 99–105.
- Avashia, V., Garg, A., Dholakia, H., 2021. Understanding temperature related health risk in context of urban land use changes. *Landscape Urban Plan.* 212, 104107.
- Bao, J., Li, X., Yu, C., 2015. The construction and validation of the heat vulnerability index, a review. *Int. J. Environ. Res. Public Health* 12 (7), 7220–7234.
- Belmin, J., Auffray, J.-C., Berbezier, C., Boirin, P., Mercier, S., de Reviers, B., Golmard, J.-L., 2007. Level of dependency: a simple marker associated with mortality during the 2003 heatwave among French dependent elderly people living in the community or in institutions. *Age Ageing* 36 (3), 298–303.
- Bowler, D.E., Buyung-Ali, L., Knight, T.M., Pullin, A.S., 2010. Urban greening to cool towns and cities: A systematic review of the empirical evidence. *Landscape Urban Plan.* 97 (3), 147–155.
- Campbell, S., Remenyi, T.A., White, C.J., Johnston, F.H., 2018. Heatwave and health impact research: A global review. *Health Place* 53, 210–218.
- Cao, B., Liu, Q., Du, Y., Roujean, J.-L., Gastellu-Etchegorry, J.-P., Trigo, I.F., Zhan, W., Yu, Y., Cheng, J., Jacob, F., 2019. A review of earth surface thermal radiation directionality observing and modeling: historical development, current status and perspectives. *Remote Sens. Environ.* 232, 111304.
- Cao, Y., Lu, Z., Chu, J., Xu, X., Zhao, Z., Geng, M., Chen, G., Hu, K., Xia, J., Liu, Q., 2023. Intraseasonal variation of the association between heat exposure and mortality risk in Shandong province, China. *Urban Clim.* 51, 101621.
- Chen, B., Xie, M., Feng, Q., Wu, R., Jiang, L., 2022. Diurnal heat exposure risk mapping and related governance zoning: A case study of Beijing, China. *Sustain. Cities Soc.* 81, 103831.
- Cheval, S., Dumitrescu, A., Iraçoc, A., Paraschiv, M.-G., Perry, M., Ghent, D., 2022. MODIS-based climatology of the surface urban Heat Island at country scale (Romania). *Urban Clim.* 41, 101056.
- Cheval, S., Dumitrescu, A., Amihăescu, V., Iraçoc, A., Paraschiv, M.-G., Ghent, D., 2023. A country scale assessment of the heat hazard-risk in urban areas. *Build. Environ.* 229, 109892.
- Crichton, D., 1999. The risk triangle. *Nat. Disaster Manag.* 102 (3), 102–103.
- Denson, E., Wasko, C., Peel, M.C., 2021. Decreases in relative humidity across Australia. *Environ. Res. Lett.* 16 (7), 074023.
- Doll, C.N., Muller, J.-P., Morley, J.G., 2006. Mapping regional economic activity from night-time light satellite imagery. *Ecol. Econ.* 57 (1), 75–92.
- Dong, J., Peng, J., He, X., Corcoran, J., Qiu, S., Wang, X., 2020. Heatwave-induced human health risk assessment in megacities based on heat stress-social vulnerability-human exposure framework. *Landscape Urban Plan.* 203, 103907.
- Elizabeth Loughnan, M., Tapper, J., Phan, T., McInnes, J., 2014. Can a spatial index of heat-related vulnerability predict emergency service demand in Australian capital cities? *Int. J. Emerg. Serv.* 3 (1), 6–33.
- Estoque, R.C., Ooba, M., Seposo, X.T., Togawa, T., Hijioka, Y., Takahashi, K., Nakamura, S., 2020. Heat health risk assessment in Philippine cities using remotely sensed data and social-ecological indicators. *Nat. Commun.* 11 (1), 1581.
- Field, C.B., Van Aalst, M., Adger, W.N., Arent, D., Barnett, J., Betts, R., Bilir, E., Birkmann, J., Carmin, J., Chadee, D., 2014. Part a: global and sectoral aspects: volume 1, global and sectoral aspects: working group II contribution to the fifth assessment report of the intergovernmental panel on climate change. In: *Climate Change 2014: impacts, adaptation, and vulnerability*. IPCC, pp. 1–1101.
- Fu, J., Dupre, K., Tavares, S., King, D., Banhami-Zakar, Z., 2022. Optimized greenery configuration to mitigate urban heat: A decade systematic review. *Front. Architect. Res.* 11 (3), 466–491.
- Ginzburg, A., Belova, I., Dokukin, S., Falaleeva, V., 2024. Wind speed trend effects on the length of the thermal comfort period in European Russia in recent decades. *Russ. Meteorol. Hydrol.* 49 (2), 106–113.
- Ho, H.C., Knudby, A., Chi, G., Aminipour, M., Lai, D.Y.-F., 2018. Spatiotemporal analysis of regional socio-economic vulnerability change associated with heat risks in Canada. *Appl. Geogr.* 95, 61–70.
- Hossain, S.M.N., 2001. Assessing Human Vulnerability Due to Environmental Change: Concepts and Assessment Methodologies. Master of Science Degree Thesis, Division of Land and Water Resources. Department of Civil and Environmental Engineering, Royal Institute of Technology, KTH, Stockholm, Sweden.
- Hu, K., Guo, Y., Yang, X., Zhong, J., Fei, F., Chen, F., Zhao, Q., Zhang, Y., Chen, G., Chen, Q., 2019. Temperature variability and mortality in rural and urban areas in Zhejiang province, China: an application of a spatiotemporal index. *Sci. Total Environ.* 647, 1044–1051.
- Hu, S., Huang, S., Hu, Q., Wang, S., Chen, Q., 2024. An commercial area extraction approach using time series nighttime light remote sensing data—take Wuhan city as a case. *Sustain. Cities Soc.* 100, 105032.
- Im, E.-S., Thanh, N.-X., Kim, Y.-H., Ahn, J.-B., 2019. 2018 summer extreme temperatures in South Korea and their intensification under 3° C global warming. *Environ. Res. Lett.* 14 (9), 094020.
- Johnson, B.A., Jozdani, S.E., 2019. Local climate zone (LCZ) map accuracy assessments should account for land cover physical characteristics that affect the local thermal environment. *Remote Sens.* 11 (20), 2420.
- Kenny, G.P., Yardley, J., Brown, C., Sigal, R.J., Jay, O., 2010. Heat stress in older individuals and patients with common chronic diseases. *Cmaj* 182 (10), 1053–1060.
- Lam, N.S.-N., Cheng, W., Zou, L., Cai, H., 2018. Effects of landscape fragmentation on land loss. *Remote Sens. Environ.* 209, 253–262.
- Lau, K.K.-L., Chung, S.C., Ren, C., 2019. Outdoor thermal comfort in different urban settings of sub-tropical high-density cities: an approach of adopting local climate zone (LCZ) classification. *Build. Environ.* 154, 227–238.
- Lloyd, S.J., Striessnig, E., Achebak, H., Hajat, S., Muttarak, R., Quijal-Zamorano, M., Rizzi, S., Vielma, C., Ballester, J., 2024. Remeasuring the influence of ageing on heat-related mortality in Spain, 1980 to 2018. *Environ. Res.* 248, 118408.
- Ma, X., Peng, S., 2022. Research on the spatiotemporal coupling relationships between land use/land cover compositions or patterns and the surface urban heat island effect. *Environ. Sci. Pollut. Res.* 29 (26), 39723–39742.
- Ma, L., Huang, G., Johnson, B.A., Chen, Z., Li, M., Yan, Z., Zhan, W., Lu, H., He, W., Lian, D., 2023. Investigating urban heat-related health risks based on local climate zones: A case study of Changzhou in China. *Sustain. Cities Soc.* 91, 104402.
- Macintyre, H.L., Heaviside, C., Cai, X., Phalkey, R., 2021. The winter urban heat island: impacts on cold-related mortality in a highly urbanized European region for present and future climate. *Environ. Int.* 154, 106530.
- Medina-Ramon, M., Schwartz, J., 2007. Temperature, temperature extremes, and mortality: a study of acclimatization and effect modification in 50 US cities. *Occup. Environ. Med.* 64 (12), 827–833.
- Michelozzi, P., De' Donato, F., 2021. IPCC sixth assessment report: stopping climate change to save our planet. *Epidemiol. Prev.* 45 (4), 227–229.
- Muccione, V., Biesbroek, R., Harper, S., Haasnoot, M., 2024. Towards a more integrated research framework for heat-related health risks and adaptation. *Lancet Planetary Health* 8 (1), e61–e67.
- Nie, J.D., Zhang, J.H., Huang, B., 2021. A review of the human health consequences of urban heat island effect. *Ecol. Sci.* 40 (1), 200–208.
- Paranunzio, R., Dwyer, E., Fitton, J.M., Alexander, P.J., O'Dwyer, B., 2021. Assessing current and future heat risk in Dublin city, Ireland. *Urban Clim.* 40, 100983.
- Peng, J., Jia, J., Liu, Y., Li, H., Wu, J., 2018. Seasonal contrast of the dominant factors for spatial distribution of land surface temperature in urban areas. *Remote Sens. Environ.* 215, 255–267.
- Peng, J., Cheng, X., Hu, Y., Corcoran, J., 2022. A landscape connectivity approach to mitigating the urban heat island effect. *Landscape Ecol.* 37 (6), 1707–1719.

- Pramanik, S., Punia, M., Yu, H., Chakraborty, S., 2022. Is dense or sprawl growth more prone to heat-related health risks? Spatial regression-based study in Delhi, India. *Sustain. Cities Soc.* 81, 103808.
- Reduction, U.N.O., f. D. R., 1901. Global Assessment Report on Disaster Risk Reduction 2022: Our World at Risk: Transforming Governance for a Resilient Future. UN.
- Romero-Lankao, P., Qin, H., Dickinson, K., 2012. Urban vulnerability to temperature-related hazards: A meta-analysis and meta-knowledge approach. *Glob. Environ. Chang.* 22 (3), 670–683.
- Sharma, A., Woodruff, S., Budhathoki, M., Hamlet, A., Chen, F., Fernando, H., 2018. Role of green roofs in reducing heat stress in vulnerable urban communities—A multidisciplinary approach. *Environ. Res. Lett.* 13 (9), 094011.
- Sherwood, S.C., Huber, M., 2010. An adaptability limit to climate change due to heat stress. *Proc. Natl. Acad. Sci.* 107 (21), 9552–9555.
- Solaimani, K., Ahmadi, S.B., Shokrian, F., 2024. The spatiotemporal trend changes of extreme temperature-humidity variables and their impact on climatic comfort changes. *Ecol. Indic.* 158, 111629.
- Soneja, S., Jiang, C., Fisher, J., Upperman, C.R., Mitchell, C., Sapkota, A., 2016. Exposure to extreme heat and precipitation events associated with increased risk of hospitalization for asthma in Maryland, USA. *Environ. Health* 15, 1–7.
- Song, J., Chen, W., Zhang, J., Huang, K., Hou, B., Prishchepov, A.V., 2020. Effects of building density on land surface temperature in China: spatial patterns and determinants. *Landsl. Urban Plan.* 198, 103794.
- Stewart, I.D., Oke, T.R., 2012. Local climate zones for urban temperature studies. *Bull. Am. Meteorol. Soc.* 93 (12), 1879–1900.
- Sun, H., Chen, Y., Li, K., Gao, S., 2024. Spatio-temporal assessment of heat health risk in Chinese metropolitan cities based on the modified multi-indicators coupled risk framework. *Sustain. Cities Soc.* 108, 105451.
- Verdonck, M.-L., Demuzere, M., Hooyberghs, H., Beck, C., Cyrys, J., Schneider, A., Dewulf, R., Van Coillie, F., 2018. The potential of local climate zones maps as a heat stress assessment tool, supported by simulated air temperature data. *Landsl. Urban Plan.* 178, 183–197.
- Verdonck, M.-L., Demuzere, M., Hooyberghs, H., Priem, F., Van Coillie, F., 2019. Heat risk assessment for the Brussels capital region under different urban planning and greenhouse gas emission scenarios. *J. Environ. Manag.* 249, 109210.
- Walton, Z., Poudyal, N., Hepinstall-Cymerman, J., Gaither, C.J., Boley, B., 2016. Exploring the role of forest resources in reducing community vulnerability to the heat effects of climate change. *Forest Policy Econ.* 71, 94–102.
- Wang, M., Zhang, Z., Hu, T., Liu, X., 2019. A practical single-channel algorithm for land surface temperature retrieval: application to landsat series data. *J. Geophys. Res. Atmos.* 124 (1), 299–316.
- Wang, M., Zhang, Z., Hu, T., Wang, G., He, G., Zhang, Z., Li, H., Wu, Z., Liu, X., 2020. An efficient framework for producing Landsat-based land surface temperature data using Google earth engine. *IEEE J. Selected Top. Appl. Earth Observ. Remote Sens.* 13, 4689–4701.
- Wang, P., Wong, Y.H., Tan, C.Y., Li, S., Chong, W.T., 2022. Vertical greening systems: technological benefits, progresses and prospects. *Sustainability* 14 (20), 12997.
- Wang, S., Cai, W., Tao, Y., Sun, Q.C., Wong, P.P.Y., Thongkong, W., Huang, X., 2023. Nexus of heat-vulnerable chronic diseases and heatwave mediated through tri-environmental interactions: A nationwide fine-grained study in Australia. *J. Environ. Manag.* 325, 116663.
- Wei, F., Hu, W., Teng, E., Wu, G., 2000. Advance of study on the impact of air pollution on human health. *World Sci. Technol. Res. Devel.* 22 (3), 14–18.
- Wolf, T., Chuang, W.-C., McGregor, G., 2015. On the science-policy bridge: do spatial heat vulnerability assessment studies influence policy? *Int. J. Environ. Res. Public Health* 12 (10), 13321–13349.
- Wu, Y., Shi, K., Chen, Z., Liu, S., Chang, Z., 2021. Developing improved time-series DMSP-OLS-like data (1992–2019) in China by integrating DMSP-OLS and SNPP-VIIRS. *IEEE Trans. Geosci. Remote Sens.* 60, 1–14.
- Wu, H., Zhao, C., Zhu, Y., Pan, Y., 2024. A multiscale examination of heat health risk inequality and its drivers in mega-urban agglomeration: A case study in the Yangtze River Delta, China. *J. Clean. Prod.* 458, 142528.
- Xiang, Y., Huang, C., Huang, X., Zhou, Z., Wang, X., 2021. Seasonal variations of the dominant factors for spatial heterogeneity and time inconsistency of land surface temperature in an urban agglomeration of Central China. *Sustain. Cities Soc.* 75, 103285.
- Xiang, Z., Qin, H., He, B.-J., Han, G., Chen, M., 2022. Heat vulnerability caused by physical and social conditions in a mountainous megacity of Chongqing, China. *Sustain. Cities Soc.* 80, 103792.
- Xiang, R., Hou, X., Li, R., 2024a. Health risks from extreme heat in China: evidence from health insurance. *J. Environ. Manag.* 354, 120300.
- Xiang, Y., Yuan, C., Cen, Q., Huang, C., Wu, C., Teng, M., Zhou, Z., 2024b. Heat risk assessment and response to green infrastructure based on local climate zones. *Build. Environ.* 248, 111040.
- Xiao, Y., Piao, Y., Wei, W., Pan, C., Lee, D., Zhao, B., 2023. A comprehensive framework of cooling effect-accessibility-urban development to assessing and planning park cooling services. *Sustain. Cities Soc.* 98, 104817.
- Xie, Y., Xu, F., Ye, Q., Zhai, Z., Yang, H., Feng, X., Shi, J., Hu, W., 2024. Spatial distribution of old neighborhoods based on heat-related health risks assessment: A case study of Changsha City, China. *Sustain. Cities Soc.* 105740.
- Xu, H., Li, C., Hu, Y., Kong, R., Wang, Q., Zhou, Y., 2024. Long-term temporal and spatial divergence patterns of urban heat risk in the Beijing–Tianjin–Hebei urban agglomeration. *Urban Clim.* 56, 102085.
- Xue, X., He, T., Xu, L., Tong, C., Ye, Y., Liu, H., Xu, D., Zheng, X., 2022. Quantifying the spatial pattern of urban heat islands and the associated cooling effect of blue-green landscapes using multisource remote sensing data. *Sci. Total Environ.* 843, 156829.
- Yang, C., Zhao, S., 2023. Diverse seasonal hysteresis of surface urban heat islands across Chinese cities: patterns and drivers. *Remote Sens. Environ.* 294, 113644.
- Yang, J., Zhou, M., Ren, Z., Li, M., Wang, B., Liu, D.L., Ou, C.-Q., Yin, P., Sun, J., Tong, S., 2021. Projecting heat-related excess mortality under climate change scenarios in China. *Nat. Commun.* 12 (1), 1039.
- Yuan, Y., Li, C., Geng, X., Yu, Z., Fan, Z., Wang, X., 2022. Natural-anthropogenic environment interactively causes the surface urban heat island intensity variations in global climate zones. *Environ. Int.* 170, 107574.
- Zhang, T., Wu, Y., 2017. Analysis of the impact of air pollution on human health and prevention methods. *Sports Fashion* 03, 164.
- Zhao, J., Chen, G., Yu, L., Ren, C., Xie, J., Chung, L., Ni, H., Gong, P., 2023. Mapping urban morphology changes in the last two decades based on local climate zone scheme: A case study of three major urban agglomerations in China. *Urban Clim.* 47, 101391.
- Zhu, W., Yuan, C., 2023. Urban heat health risk assessment in Singapore to support resilient urban design—by integrating urban heat and the distribution of the elderly population. *Cities* 132, 104103.